

Global Characteristics of Oceanic Transform Fault Structure and Seismicity

Monica Wolfson-Schwehr^{*}, Margaret S. Boettcher[†]

^{*}Monterey Bay Aquarium Research Institute, Moss Landing, CA, United States [†]Department of Earth Sciences, University of New Hampshire, Durham, NH, United States

OUTLINE

1 Introduction	21	4 The Effect of Fault Structure on the Seismicity	41
1.1 Background	22		
2 Global Characterization of Oceanic Transform Fault Structure	28	5 Conclusion	55
3 Updated Global Characterization of Oceanic Transform Fault Seismicity	39	Acknowledgments	56
		References	56
		Further Reading	59

1 INTRODUCTION

Mid-ocean ridge transform faults (RTFs), which are bounded by two ridge segments, have historically been viewed as geometrically simple (Wilson, 1965b; Menard and Atwater, 1968; Fox and Gallo, 1984; Sandwell, 1986; Fox and Gallo, 1989). With fault lengths readily obtained from ridge-transform intersections (RTIs) and slip rates easily determined from global models, RTFs have been viewed as an ideal environment for studying strike-slip earthquake behavior (e.g., Parson and Searle, 1986; Boettcher and Jordan, 2004; Willoughby and Hyndman, 2005; Gregg et al., 2006; Roland and McGuire, 2009; McGuire et al., 2012; Sykes

and Ekström, 2012). Despite the recent attention they have received, there are still many facets of seismic behavior on RTFs that are not well understood. Two aspects of RTF seismicity driving current research are as follows:

- (1) RTFs have large seismic moment deficits, indicating that the majority of slip is accommodated aseismically. What controls the distribution of seismic coupling, the proportion of slip on the fault accommodated seismically, along RTFs?
- (2) Earthquakes on RTFs are small compared to their seismogenic area. What prevents the largest events from rupturing the full fault area?

A possible explanation for the observations of along-strike variability in seismic coupling and small maximum magnitudes on RTFs is segmentation of the fault trace. Physical segmentation occurs when the fault trace is divided into a series of two or more parallel to subparallel fault strands, separated by step-overs that are predominately extensional basins or intra-transform spreading centers (ITSCs). By contrast, mechanical segmentation occurs when properties, such as composition, permeability, and damage intensity, vary along strike. While global bathymetric data compilations (Smith and Sandwell, 1997; Ryan et al., 2009; Sandwell et al., 2014), high-resolution multibeam bathymetry, and sidescan sonar surveys (Lonsdale, 1978; Madsen et al., 1986; Fornari et al., 1989; Embley and Wilson, 1992; Goff et al., 1993; Pockalny et al., 1997; Gallo et al., 2012) have shown that the geometry of RTFs is more complex than has been traditionally viewed, physical segmentation on scales less than ~35 km has not yet been considered in global RTF studies. Similarly, only a few studies of individual RTFs (e.g., Van Avendonk et al., 2001; McGuire et al., 2012; Wolfson-Schwehr et al., 2014; Kuna et al., 2017) have had enough resolution to detect along-strike changes in fault zone mechanical properties; therefore, mechanical segmentation, like physical segmentation, thus far has not been included in global RTF studies.

This chapter presents a global characterization of oceanic transform fault structure and investigates whether physical segmentation can explain the low seismic coupling on RTFs (on average, ~15% of motion is accommodated seismically; Boettcher and Jordan, 2004), small maximum RTF earthquake sizes, and the location of RTF repeating rupture patches that are currently observed. One hypothesis is that by accounting for physical fault segmentation, the seismogenic area will be more accurately calculated, resulting in an increased seismic coupling and an increased proportion of the seismogenic area ruptured by the largest earthquakes.

1.1 Background

1.1.1 Early Studies of Oceanic Transform Faults and the Evolution Seafloor Mapping

Early studies of RTF structure relied on towed seismic surveys, gravity and magnetics data (e.g., Wilson, 1965a, b; Hey, 1977; Bird et al., 1998), sidescan sonar (e.g., Searle, 1986; Taylor et al., 1994), and singlebeam echosounders (e.g., Macdonald et al., 1979). These data provided profound insight into the structure and tectonics of a few RTFs. The pattern of magnetic anomaly offsets observed across RTFs confirmed the hypothesis of transform motion between bounding ridge segments (Wilson, 1965b; Hey, 1977). Sidescan sonar data showed that the fault zone could be made up of several fault strands oriented approximately parallel to slip direction,

and that RTFs could be spaced close together and oriented oblique to the spreading direction (Searle, 1984, 1986). The combined use of sidescan sonars and singlebeam echosounders on the Vema Transform Fault, on the Mid-Atlantic Ridge (MAR) showed the presence of both median ridges and valleys, and showed that the width of the fault zone may vary along a transform fault, often narrowing away from the RTI (Macdonald et al., 1979). These early studies were significant, but were limited in resolution and scope, only covering a few transform faults. More recent surveys have utilized higher-resolution multibeam sonars, capable of mapping at the resolution of a couple hundred meters or less (e.g., Fornari et al., 1989; Embley and Wilson, 1992; Goff et al., 1993; Lonsdale, 1994; Dziak et al., 2000; Pickle et al., 2009). Despite the higher resolution and increased detail in the resulting maps, these surveys also sampled only a few RTFs, rather than providing a global understanding of RTF structure.

Recent global bathymetric data compilations that integrate satellite topography and higher resolution shipborne data allowed more detailed analysis of RTF structure on a global scale (e.g., Smith and Sandwell, 1997; Ryan et al., 2009; Sandwell et al., 2014). However, the resolution of global grids is highly variable. In areas where no shipborne sonar data are available, the resolution is controlled by the limitations of satellite altimetry and the methodology used to obtain the predictions of seafloor depth, such that the grid resolution is often higher than the data resolution. In areas where high-resolution shipborne sonar data have been incorporated, the resolution of the data are generally higher than that of the global grid, and the grid drastically undersamples the data. In both cases, the resolvability of features on the seafloor is affected. Therefore, in this study, we supplement the global grids with stand-alone, high-resolution shipborne sonar surveys, where available, to generate our global characterization of oceanic transform fault structure.

To illustrate the importance of continued high-resolution mapping of the seafloor, Fig. 1 presents a progression of data resolution over the same patch of the seafloor, centered at 4°S on the East Pacific Rise (EPR), mapped from different datasets. In the top panel, the mid-ocean ridge (MOR) system is discernible, but the number and structure of RTFs are not. This panel shows predicted bathymetry from the Smith and Sandwell Global Topography dataset without shipborne sonar data, and thus seafloor features closer together, or smaller than, ~12.5km, are hard to resolve. The data in the top panel are gridded at 1-arcmin, significantly oversampling the data. Only about 10% of the oceans have been mapped by shipborne sonar data at a resolution of 1-arcmin (Becker et al., 2009). Therefore, the data resolution in the top panel is representative of 90% of the world's seafloor. The middle panel shows the same region of the seafloor, also mapped from the Smith and Sandwell Global Topography dataset, with the shipborne sonar data included. The view of the MOR system is much clearer and RTFs can be more readily discerned, though the detail of their structure remains hard to resolve. The shipborne data is of much higher resolution (200m) than the resolution of the grid (1 arcmin), therefore the grid itself becomes the limiting factor on the data resolution. The bottom panel shows shipborne multibeam sonar data of the same region, gridded at a resolution of 200m. Three distinct, physically segmented RTF systems can be discerned, each composed of two or more individual fault strands. Situated just north of the middle fault system is a block of seafloor that appears to be rotated counterclockwise, comprising a possible nanoplate (Forsyth et al., 2007; Wolfson-Schwehr et al., 2014). It is clear from this progression that while global bathymetric grids provide useful information for studying the seafloor, shipborne sonar is required to more fully characterize the complexity of seafloor structures and investigate the details of plate tectonic processes.

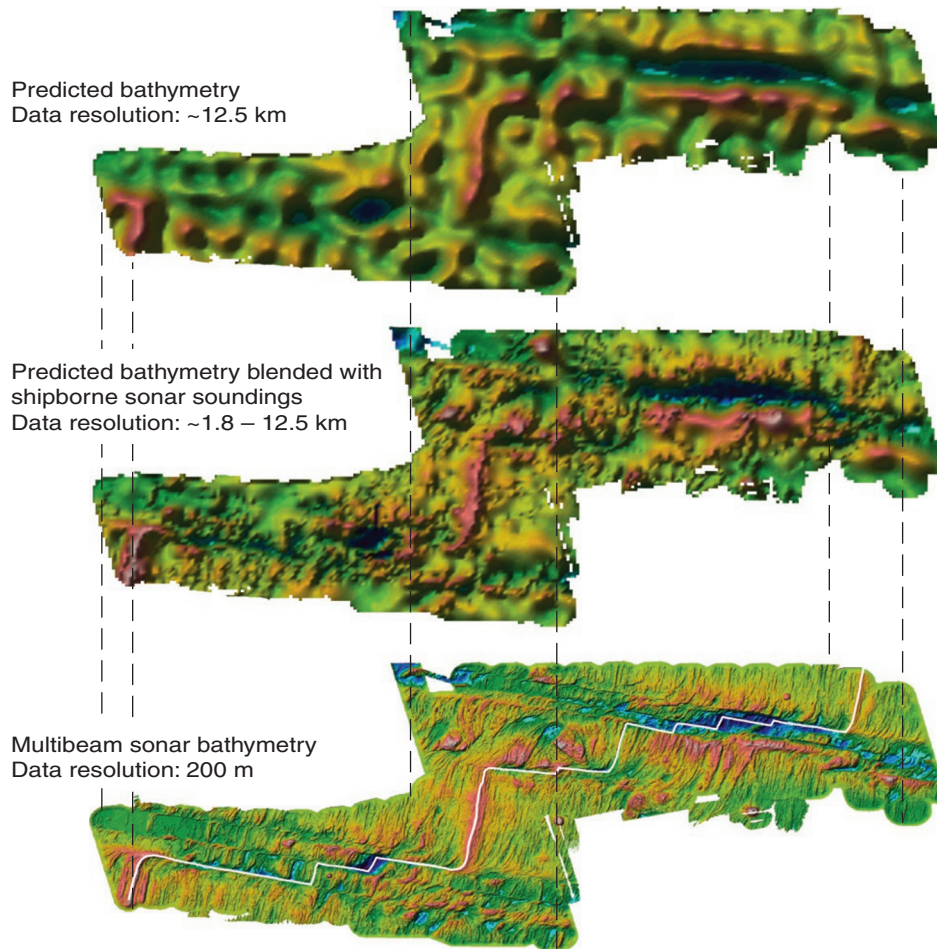


FIG. 1 Increasing progression of data resolution, from predicted bathymetry to multibeam sonar bathymetry, showing the true complexity of the Quebrada, Discovery, and Gofar transform fault system, located at 4°S on the East Pacific Rise (EPR). Data credits: Top panel: Smith & Sandwell Global Topography dataset (Smith and Sandwell, 1997). Data shown are the predicted bathymetric values only. Middle panel: The Smith and Sandwell Global Topography dataset showing the predicted bathymetry blended with data from high-resolution shipborne sonar data. Bottom image: SeaBeam 2112 survey conducted in 2006. Plate boundary from Pickle et al. (2009).

1.1.2 Physical Segmentation of Mid-Ocean Ridge Transform Faults

Physical segmentation (herein just referred to as segmentation) of an RTF divides the fault into parallel or subparallel fault segments, which are laterally offset from one another by either a fault step, extensional basin, or ITSC (Gregg et al., 2006, 2009; Wolfson-Schwehr et al., 2014). The physical breakup of the fault into multiple strands is thought to occur primarily as a response to changes in plate-motion direction that create extension across the fault (Menard and Atwater, 1968; Fox and Gallo, 1989; Lonsdale, 1994; Pockalny et al., 1997; Gregg et al., 2006). On intermediate- and fast-slipping faults, where the lithosphere

is hot and thin, extension can lead to the formation of fissures near the fault trace that allow melt to extrude, resulting in what is known as a “leaky” transform fault (Kastens et al., 1979; Murton, 1986; Searle, 1986). Under continued extension, the fissures may coalesce, forming pull-apart basins and eventually ITSCs (e.g., the Siqueiros Transform Fault, Fig. 2; Pockalny et al., 1997). On slower slipping RTFs, where the lithosphere is thicker and colder, extension may lead to the formation of basins in which the extension is primarily accommodated through normal faulting (Embley and Wilson, 1992). Alternatively, ITSCs may also form due to compression. For example, it is hypothesized that a spreading ridge was entrained into the transform domain during rift propagation with a change in plate motion, creating the Cascadia Depression on the Blanco Transform Fault (Braunmiller and Nábělek, 2008).

Fig. 2 shows an illustration of the effects of changes in plate motion for the Clipperton and Siqueiros transform faults, 10°N and 8°N on the EPR, respectively. Recent (over the last $\sim 2\text{--}3\text{ m/yr}$) $1\text{--}5$ degree counterclockwise changes in spreading direction between the Pacific and Cocos plates (Carbotte and Macdonald, 1994) put the left-lateral Clipperton Transform Fault under transpression, while the right-lateral Siqueiros Transform Fault was put under

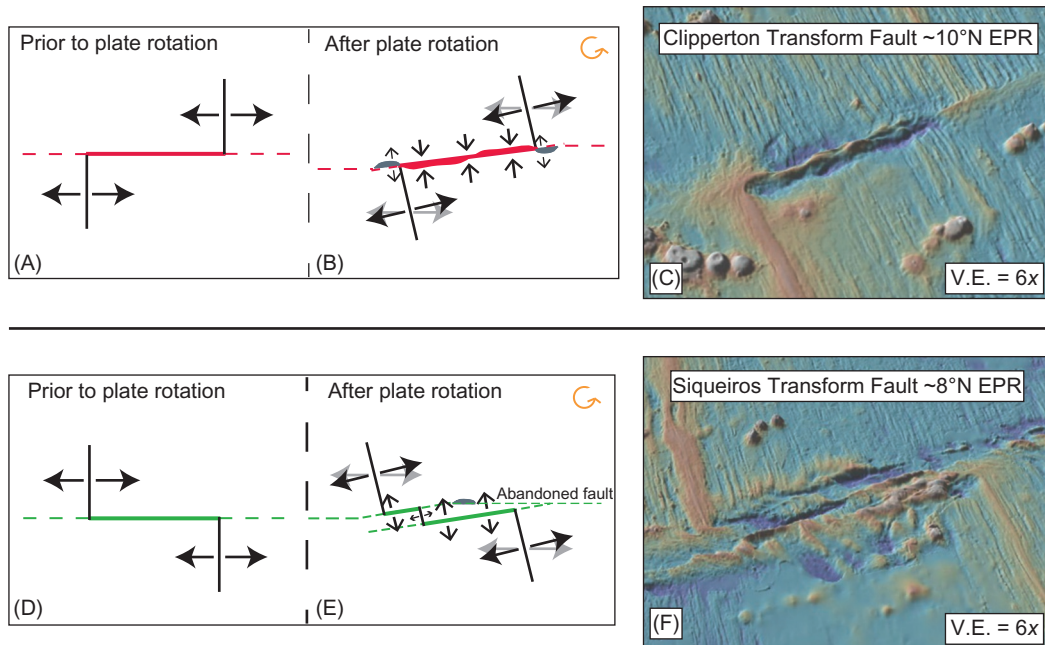


FIG. 2 (A) Left-lateral transform fault. (B) The fault in (a) during a counterclockwise change in plate motion direction, with compressional and extensional stresses experienced by the fault during the adjustment (arrows). The red thickened zones on either side of the transform represent compressional ridges. The gray patches represent extensional transverse ridges. (C) The Clipperton Transform Fault, a real-world example of the fault depicted in (a) and (b). (D) Right-lateral transform fault. (E) The fault in (d) during a counterclockwise change in the direction of plate motion with resulting extensional stresses (arrows). Extension along the fracture zones and abandoned fault traces may lead to normal faulting and the formation of extensional ridges on the older side of the fault (gray patches). (F) The Siqueiros Transform Fault, a real-world example of the fault depicted in (d) and (e). Figure is based on Pockalny et al. (1997).

transtension (Macdonald et al., 1992; Pockalny, 1997; Pockalny et al., 1997). Compression prevented the Clipperton transform and nearby ridges from quickly adjusting to the new plate motion, resulting in a period of spreading oriented between the new and the old directions. Compression also caused the formation of median ridges along the fault (Pockalny, 1997) and anomalously rotated abyssal hill fabric on either side of the fault (Sonder and Pockalny, 1999; Croon et al., 2010). The younger side of the inactive fracture zone realigned to the new spreading direction relatively quickly, while the older side, which is colder and denser, took longer. This discrepancy led to a zone of extension at the RTI, resulting in fissures and melt extrusion that form the RTI highs that are visible today. On Siqueiros, the extension across the fault zone led to the formation of fissures and melt extrusion as described above, resulting in the development of ITSCs. Over the course of a few million years, continued counterclockwise shifts in the spreading direction resulted in the segmentation of the Siqueiros Transform Fault into a series of subparallel fault strands (Fig. 2; Pockalny et al., 1997).

1.1.3 Mid-Ocean Ridge Transform Fault Seismicity

Slip along RTFs is accommodated by both seismic and aseismic processes, with the majority of slip occurring aseismically (e.g., Brune, 1968; Bird et al., 2002; Boettcher and Jordan, 2004; Frohlich and Wetzell, 2007). The seismicity appears to be strongly controlled by the underlying thermal structure, where RTF earthquake focal depths (Abercrombie and Ekström, 2001; Braunmiller and Nábělek, 2008; Roland et al., 2010) combined with results from laboratory friction experiments (Boettcher et al., 2007; King and Marone, 2012) indicate that the seismogenic zone is limited by approximately the 600°C isotherm.

Boettcher and Jordan (2004) computed a set of global scaling relations for RTFs that relate the thermal structure to both the largest expected earthquake (M_C) and the total seismic moment ($\sum M$). Combining the length (L) and slip rate (V), the seismogenic area (A_T) can be calculated using the half-space cooling model:

$$A_T = C_T L^{3/2} V^{-1/2} \quad (1)$$

where the constant, C_T , depends on the reference isotherm chosen as the base of the seismogenic zone ($C_T = 4.1 \times 10^{-3} \text{ km/yr}^{(1/2)}$, for 600°C). Boettcher and McGuire (2009) revisited the scaling relations, using an additional 10 years of data, and added a new scaling relation for the expected duration of seismic cycles on RTFs. The results from these studies indicate that there is a global seismic moment deficit on RTFs, and the largest earthquakes do not rupture the full fault area (Boettcher and Jordan, 2004; Boettcher et al., 2009). Boettcher and Jordan (2004) proposed four models for the partitioning of seismic and aseismic slip on RTFs:

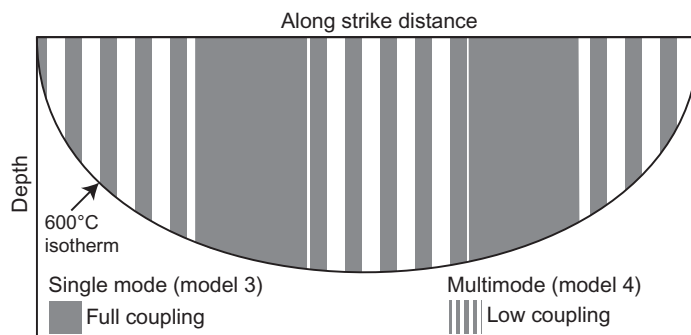
1. *Single-mode, thin, shallow seismogenic zone*, where each part of the fault is either fully seismically coupled or fully aseismic. In this model the seismogenic zone is thin and shallow. It is fully coupled, while the remainder of the fault below the seismogenic zone is fully aseismic. If the upper boundary of the seismogenic zone is taken to be the seafloor, then Boettcher and Jordan's (2004) scaling relations constrain the depth limit of seismic slip to roughly coincide with the 150°C isotherm. Consequently, this model has been rejected because seismicity is known to nucleate down to 600°C (e.g., Braunmiller and Nábělek, 2008; Roland et al., 2010).

2. *Single-mode, thin, deep seismogenic zone*, where a thin, fully coupled seismogenic zone is located deeper within the lithosphere. If the base of the seismogenic zone is fixed at the 600°C isotherm, then the scaling relations of Boettcher and Jordan suggest that the top of the seismogenic zone would correspond with the 520°C isotherm, which approximates the extent of the serpentinite and talc stability zones. Both minerals may exhibit velocity-strengthening behavior, therefore the presence of these alteration phases in the shallow lithosphere may inhibit earthquake nucleation. This model is also considered unlikely, based on ocean bottom seismic studies that found earthquake hypocenters at temperatures $\geq 200^\circ\text{C}$ (Roland et al., 2012).
3. *Single-mode, thick seismogenic patches*, where the seismogenic zone is divided into multiple patches along strike, such that a particular patch of the fault is either fully seismic or fully aseismic. The area of each fully coupled patch is determined by the area of the fault ruptured by largest repeating earthquake. The patches may extend from the seafloor down to the 600°C isotherm. As described in detail below, there is mounting evidence that the largest earthquakes on many RTFs occur on fully coupled patches, and thus aspects of this model closely reflect recent observations of RTF seismicity.
4. *Multimode fault*, where slip can occur either seismically or aseismically over the full area above the 600°C isotherm; thus, no portion of the fault is fully coupled. Evidence for multimode behavior, also known as intermediate coupling, comes from observations of (1) fault patches wherein only microseismic activity appears to occur (McGuire et al., 2012), (2) large earthquakes that occur in moderate or low seismic coupling zones (e.g., magnitude >6 earthquakes occur infrequently on the western portion of Blanco Transform Fault; Braunmiller and Nábělek, 2008), and (3) from three-dimensional strike-slip rate-and-state friction models in which RTF segments transition between seismic and aseismic slip over many earthquake cycles (Liu et al., 2012).

Lending credence to models 3 and 4, the largest expected earthquakes on a number of RTFs have been observed to repeatedly rupture the same fault patch, including on Gofar and Discovery on the EPR (McGuire, 2008; Wolfson-Schwehr et al., 2014), the Eltanin fault system (Heezen, Tharp, and Hollister transform faults) on the Pacific-Antarctic Ridge (PAR) (Sykes and Ekström, 2012), Charlie Gibbs on the MAR (Aderhold and Abercrombie, 2016), and Blanco on the Juan de Fuca Ridge (JdFR) (Braunmiller and Nábělek, 2008; Boettcher and McGuire, 2009). Seismic coupling along these faults is highly variable along strike, with the majority of large earthquakes rupturing fully coupled patches, separated by multimode zones characterized by low to intermediate seismic coupling.

On the Discovery and Gofar transform faults, for example, relocated $M_W > 5.4$ earthquakes from the Global Centroid Moment Tensor (CMT) catalog, combined with a yearlong ocean bottom seismometer (OBS) deployment, have shown that seismic coupling can vary significantly along strike. McGuire (2008) used a surface wave relative relocation technique and found that all of the $M_W \geq 5.5$ earthquakes on many fast-slipping EPR faults, between January 1993 and March 2008, fall into distinct rupture patches, with repeat times of $\sim 5\text{--}7$ years. A yearlong OBS deployment on Gofar (McGuire et al., 2012) showed that the foreshocks preceding the 2008 Gofar $M_W 6.0$ event occurred in a 10-km long patch of the fault just east of the main rupture patch. This foreshock zone acted as a barrier to rupture propagation during the mainshock and is associated with a zone of high porosity. Similarly, Wolfson-Schwehr et al. (2014) observed distinct rupture patches on the Discovery Transform Fault, separated by zones defined primarily by microseismic events. The repeating large rupture patches on Gofar and

FIG. 3 Conceptual model of seismic coupling on RTFs. The seismogenic area is bounded by the 600°C isotherm. Fully coupled patches repeatedly rupture during the maximum-sized earthquakes (*solid gray patches*). Zones of low to intermediate coupling (*gray and white stripes*) separate the fully coupled patches and accommodate slip via creep and microseismicity.



Discovery appear to be fully coupled, while the microseismic zones in between show relatively low coupling.

On the Blanco Transform Fault, which offsets the EPR from the JdFR, the Blanco Ridge segment of the fault hosts the majority of $M_W > 6.0$ earthquakes in two distinct, fully coupled zones that are each surrounded by regions of intermediate to low coupling (Braunmiller and Nábělek, 2008; Boettcher and McGuire, 2009). A recent OBS study on Blanco found little microseismicity in the fully coupled rupture patches on Blanco Ridge, and abundant microseismicity, driven by aseismic loading, in the surrounding regions (Kuna et al., 2017). Gofar, Discovery, and Blanco all appear to follow a combination of models 3 and 4 described above, with fully coupled patches that rupture during the largest earthquakes separated by multimode zones that accommodate motion via episodic creep and/or swarms of smaller earthquakes. Therefore, we propose that seismic coupling along RTFs follows a combination of model 3 and model 4, as illustrated in Fig. 3.

The observation that the largest repeating earthquakes on RTFs tend to repeatedly rupture the same fault patch has led to questions about what processes, or structural features, may control the size and the location of these patches. The endpoints of the large rupture patches on these faults do not always correspond with observable, lateral offsets, or step-overs, in the fault trace. Instead, they are often associated with small structural features that may be associated with stress concentrations during rupture propagation (e.g., Wolfson-Schwehr et al., 2014). These localized stress concentrations may, in turn, cause an increase in the width, or intensity, of the damage zone. We hypothesize that enhanced fracturing in the vicinity of small structural features may allow for increased porosity (e.g., Roland et al., 2012; Froment et al., 2014) and subsequent dilatant strengthening during large events, providing a mechanism for halting rupture propagation. This hypothesis supports a model of seismic slip on RTFs, which is a mix of models 3 and 4 presented in Boettcher and Jordan (2004), as is shown in Fig. 3.

2 GLOBAL CHARACTERIZATION OF OCEANIC TRANSFORM FAULT STRUCTURE

To better determine the resolution of structural complexity on oceanic transform faults in general, as well as the effect this complexity may have on the global scaling relations for RTFs, fault structure was delineated on a global scale. The primary datasets used for this

characterization were the Smith and Sandwell Global Topography dataset (v. 18.1), and the Global Multi-Resolution Topography (GMRT) synthesis (Ryan et al., 2009), which includes multibeam sonar bathymetry gridded at a variety of resolutions, gridded bathymetry from the General Bathymetric Chart of the Oceans (GEBCO_2014, v. 20141103) at a resolution of 30 arc-seconds (~ 1 km at the equator), and gridded bathymetry from the International Bathymetric Chart of the Arctic Ocean (IBCAO, v. 2.23) at a 2-km resolution. All gridded data were unprojected and displayed using the World Geodetic System (WGS) 84 ellipsoid in ArcGIS (v. 10.3), and all measurements were computed using the geodesic length. Literature searches were also conducted to find any previous structural interpretations of the transform faults included in this analysis. Slip rates were obtained from the Global Strain Rate Map Project (GSRM, v. 1.2; Kreemer et al., 2000).

Oceanic transform faults were included in the compilation if they were easily discernible in the bathymetry data and had clearly resolved endpoints. For each fault, the proportion of median ridge to median valley was estimated, and the presence of fracture zones, abyssal hill fabric, and transverse ridges were noted. For segmented fault systems, the number and length of individual fault segments and their corresponding offsets were measured. Adjacent faults were considered segments of the same fault system if the adjoining step-over is shorter than the length of either fault segment and less than 50 km. Three-dimensional finite element modeling of fault thermal structure shows that adjacent fault segments will always be thermally decoupled at distances of 50 km, irrespective of segment length or slip rate (Wolfson-Schwehr et al., 2017). Specifically, the length of the step-over (L_S) required to thermally decouple adjacent fault segments, such that the thermal area of one fault segment does not influence the thermal area of the adjacent segment, is dependent only on the length of each fault segment (L_1 and L_2), and the slip rate (V) (Fig. 4), such that a critical step-over length, L_S , is given by

$$\tilde{L}_S = C_O \frac{L_1^{1.5} + L_2^{1.5} - 0.1|L_1 - L_2|^{1.5}}{L_1 + L_2} V^{-0.6} \quad (2)$$

where C_O is a constant and thermal decoupling occurs when $L_S \geq 4\tilde{L}_S$.

This study presents a structural characterization of 204 individual fault segments mapped throughout the globe (Fig. 4, Table 1). Unsegmented faults account for 96 of these segments, while the remaining 108 fault segments are grouped into 37 segmented fault systems. Segmentation is most prevalent on the EPR, where 9 of the 11 faults are segmented fault systems ($\sim 82\%$), while along the MAR, 9 of the 35 RTFs are segmented ($\sim 26\%$). Segmented fault systems are observed across the range of MOR spreading rates, from <20 mm/yr to >130 mm/yr, however, unsegmented faults are not observed (Fig. 4C). The Clipperton Transform Fault on the EPR, at a slip rate of ~ 106 mm/yr, is the only single-segment fault with a slip rate of above ~ 90 mm/yr, which is the transition from intermediate to fast spreading (Dick et al., 2003). The EPR has undergone multiple, small (1- to 5-degree), counterclockwise changes in plate-motion direction over the last few millions of years (Macdonald et al., 1984, 1992; Carbotte and Macdonald, 1994), and the resulting transtensional stresses (Fig. 2) are likely the cause of much of the observed segmentation at fast spreading rates (Fig. 4C).

Many seafloor features provide clues to the stress state and plate motion changes that a RTF has undergone. For each transform fault, we identify (1) the proportion of median ridge

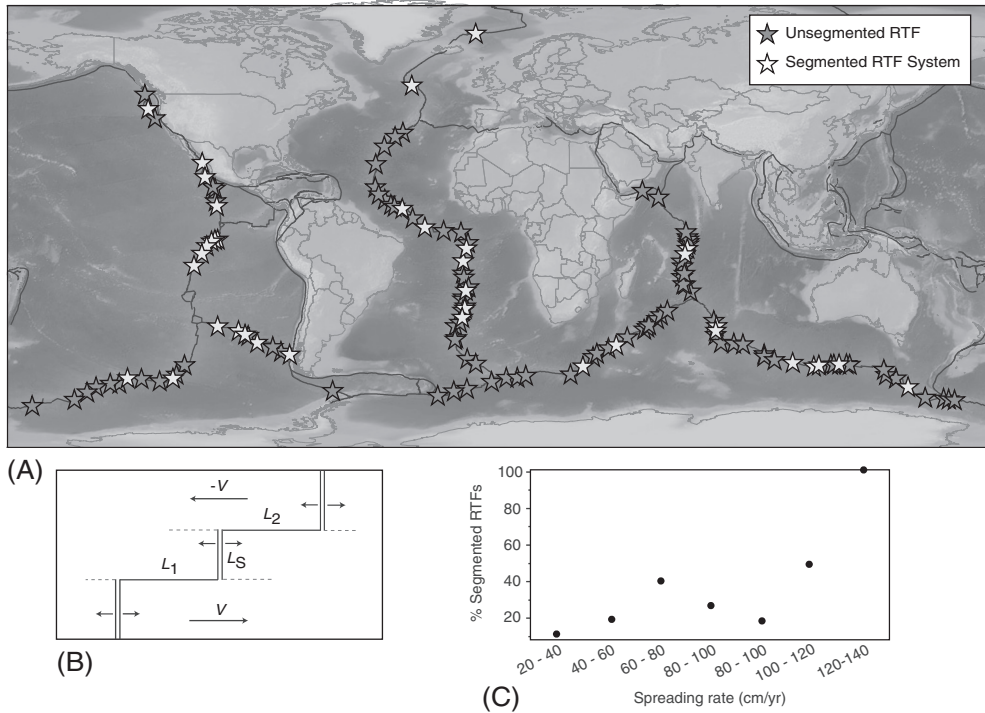


FIG. 4 (A) Global map showing the location 133 fault systems, including 37 segmented (*white stars*) and 96 unsegmented (*dark gray stars*) MOR transform faults. Map data derived from the Smith and Sandwell Global Topography dataset (ver. 18.1; [Smith and Sandwell, 1997](#)). Plate boundary model from the PLATES Project ([Coffin et al., 1998](#)). (B) Schematic of a segmented fault system spreading at rate V with fault segments of length L_1 and L_2 , offset by a step-over of length L_S . (C) Percentage of segmented RTFs binned by MOR spreading rate.

to median valley, (2) the presence, or lack, of discernable fracture zones, (3) the presence and type, normal vs anomalous, of abyssal hill fabric, and (4) the presence of transverse ridges. These features are described in more detail below and are included in the structural characterization in [Table 1](#).

The majority of transform faults are defined by median valleys, indicating that the fault is either in equilibrium with the current plate-motion direction or is under transtension. Faults may also be composed of median ridges, which form primarily as a response to increased transpression along the transform fault during periods of compression ([Pockalny, 1997](#); [Pockalny et al., 1997](#)). Some faults have a mixture of median ridge and median valley, suggesting alternating periods of transpression and transtension in the fault's past. In the case of the Sovanco Transform Fault (49°N on the JdFR), the fault zone is primarily composed of rotated crustal blocks bounded by right-lateral strike-slip faults ([Cowan et al., 1986](#)), which we denote as “complex” in the characterization. The crustal blocks are separated by northeast-trending left-lateral strike-slip faults, which [Cowan et al. \(1986\)](#) interpreted to be reactivated ridge-parallel normal faults.

Fracture zones are typically prominent linear features that extend outside RTIs. The longer the fracture zone, the longer the fault has been active and the more cumulative offset it has

TABLE 1 Structural Characterization of Global Oceanic Transform Faults

Fault # ^a	Name	Latitude	Longitude	Length (km)	Slip Rate (mm/yr)	Ridge/Valley	Fracture Zones ^b	Abyssal Hills ^b	Transverse Ridges ^b
AMERICA ANTARCTIC RIDGE									
1	Bullard A	-59.1299	-17.1358	95	12.99	Valley	Yes	c.d.	c.d.
2	Bullard B	-58.1845	-11.4861	526	13.43	Valley	Yes	c.d.	c.d.
3	Conrad	-55.7107	-3.1638	198	14.51	Valley	Yes	c.d.	Yes
4	South Sandwich	-60.8490	-22.8786	383	12.26	Valley	Yes	c.d.	no
ADEN RIDGE									
5	Alula Fartak	13.9416	51.7064	203	18.90	Valley	Yes	No	Yes
6	Owen	11.4232	57.5424	335	22.84	Valley	Yes	c.d.	c.d.
CHILE RISE									
7.1	Challenger A	-36.9977	-96.6218	78	46.56	Valley	Yes	Yes	No
7.2	Challenger B	-37.1051	-95.7193	67	46.58	Valley	Yes	Yes	No
7.3	Challenger C	-37.2455	-95.1854	20	46.61	Valley	Yes	Yes	No
7.4	Challenger D	-37.3206	-94.5776	82	46.62	Valley	Yes	Yes	No
8.1	Chile 38S A	-38.3337	-93.6255	43	46.85	Valley	Yes	Yes	No
8.2	Chile 38S B	-38.4119	-92.9817	68	46.86	Ridge	Yes	Yes	Yes
9	Chile 39S	-38.9649	-92.0683	84	46.98	Valley	Yes	Yes	No
10.1	Chile A	-35.1408	-106.5120	493	46.42	Valley	Yes	c.d.	c.d.
10.2	Chile B	-35.8981	-102.7915	186	46.46	Valley	Yes	c.d.	c.d.
10.3	Chile C	-36.2066	-99.4233	420	46.43	Valley	Yes	c.d.	c.d.
11	Chiloe	-43.0261	-83.0813	61	47.82	Valley	Yes	Yes	No
12.1	Darwin	-45.8952	-76.3639	53	48.30	Valley	Yes	Yes	No
12.2	Guamblin	-45.7052	-77.3701	80	48.27	Valley	Yes	Yes	No
13	Guafo	-44.6952	-80.1486	286	48.10	Valley	Yes	c.d.	c.d.
14.1	Valdavia A	-41.0899	-91.5642	49	47.42	Valley	Yes	Yes	No
14.2	Valdavia B	-41.1975	-90.8074	77	47.45	Valley	Yes	Yes	No
14.3	Valdavia C	-41.3049	-89.7437	97	47.47	Valley	Yes	Yes	No
14.4	Valdavia D	-41.3474	-88.4437	119	47.48	Valley	Yes	Yes	No
14.5	Valdavia E	-41.4080	-86.7164	165	47.51	Valley	Yes	Yes	No
14.6	Valdavia F	-41.4853	-85.1446	69	47.54	Valley	Yes	Yes	yes
14.7	Valdavia G	-41.5714	-84.5249	23	47.56	Valley	Yes	Yes	Yes

Continued

TABLE 1 Structural Characterization of Global Oceanic Transform Faults—Cont'd

Fault # ^a	Name	Latitude	Longitude	Length (km)	Slip Rate (mm/yr)	Ridge/ Valley	Fracture Zones ^b	Abyssal Hills ^b	Transverse Ridges ^b
CENTRAL INDIAN RIDGE									
15	Argo	−13.5851	66.3508	102	33.33	Valley	Yes	c.d.	c.d.
16.1	CIR 10S	−10.0862	66.5586	76	30.95	Valley	Yes	c.d.	c.d.
16.2	Vema II	−8.9231	67.4427	237	30.63	Valley	Yes	Yes	c.d.
17	CIR 12 12	−11.8548	65.9932	106	31.90	Valley	Yes	c.d.	c.d.
18	CIR 16S	−16.2924	66.9738	110	35.58	Valley	Yes	c.d.	c.d.
19	CIR 1S	−1.1861	67.5232	50	29.87	Valley	Yes	c.d.	c.d.
20	CIR 5S	−4.7309	68.5886	49	31.00	Valley	Yes	c.d.	c.d.
21.1	CIR 6S	−6.8331	68.2378	89	31.35	Valley	Yes	c.d.	c.d.
21.2	CIR 7S	−7.6133	68.0794	62	30.17	Valley	Yes	c.d.	c.d.
22	Egeria	−20.1347	66.5795	46	38.13	Valley	Yes	Yes	c.d.
23	Flinders	−20.2447	67.2598	65	38.48	Valley	Yes	c.d.	c.d.
24	Gemino	−22.7804	69.2857	38	40.99	Ridge	Yes	c.d.	c.d.
25	Mabahiss	−3.0415	68.1212	42	30.48	Valley	Yes	c.d.	c.d.
26	Marie Celeste	−17.5098	66.0021	219	35.99	Valley	Yes	Yes	Yes
27	Sealark	−3.8789	68.4740	63	30.78	Valley	Yes	c.d.	c.d.
28	Vityaz	−5.6877	68.3685	105	31.14	Valley	Yes	c.d.	c.d.
EAST PACIFIC RISE									
29	Clipperton	10.2195	−103.9470	84	106.28	Ridge	Yes	Anomalous	Yes
30.1	Discovery A	−4.0067	−104.3510	36	123.55	Valley	No	Yes	No
30.2	Discovery B	−3.9981	−104.0080	27	123.48	Valley	No	Yes	No
31.1	Garrett A	−13.4112	−112.1545	39	133.99	Valley	Yes	Yes	No
31.2	Garrett B	−13.4240	−111.8215	26	133.94	Valley	Yes	Yes	No
31.3	Garrett C	−13.4496	−111.5255	32	133.90	Valley	Yes	Yes	No
31.4	Garrett D	−13.4760	−111.2430	27	133.86	Valley	Yes	Yes	No
32.1	Goc 24N A	24.2430	−109.0481	61	50.37	Valley	No	No	No
32.2	Goc 24N B	23.7697	−108.5794	63	50.37	Valley	No	No	No
32.3	Goc 25N	24.9837	−109.5170	119	49.85	30/70	No	No	No
32.4	Tomayo	23.0780	−108.3355	65	50.95	Valley	Yes	Yes	Yes

TABLE 1 Structural Characterization of Global Oceanic Transform Faults—Cont'd

Fault # ^a	Name	Latitude	Longitude	Length (km)	Slip Rate (mm/yr)	Ridge/Valley	Fracture Zones ^b	Abyssal Hills ^b	Transverse Ridges ^b
33.1	Gofar A	-4.5939	-105.8490	95	124.55	Valley	Yes	Yes	No
33.2	Gofar B	-4.5792	-105.2640	29	124.40	Valley	Yes	Yes	No
33.3	Gofar C	-4.5562	-104.8820	46	124.30	Valley	Yes	Yes	No
34	Orozco A	15.4137	-105.1145	46	87.81	Valley	No	Yes	No
35	Orozco B	15.1573	-104.5815	23	88.85	Valley	No	Yes	No
36.1	Quebrada A	-3.7447	-103.6830	27	123.12	Valley	Yes	Yes	No
36.2	Quebrada B	-3.7325	-103.4445	22	123.05	Valley	Yes	Yes	No
36.3	Quebrada C	-3.7005	-103.1895	27	122.97	Valley	Yes	Yes	No
36.4	Quebrada D	-3.7302	-102.8605	42	122.94	Valley	Yes	Yes	No
37.1	Rivera A	19.5693	-108.6785	177	73.00	Valley	No	Yes	Yes
37.2	Rivera B	18.7629	-107.1555	197	73.00	Valley	Yes	Yes	No
38.1	Siqueiros A	8.3925	-104.0053	24	112.24	Valley	Yes	Yes	Yes
38.2	Siqueiros B	8.4404	-103.6818	34	112.48	Valley	Yes	Yes	Yes
38.3	Siqueiros C	8.4805	-103.4112	18	112.68	Valley	No	Yes	Yes
38.4	Siqueiros D	8.5105	-103.2089	17	112.89	Ridge	No	Yes	Yes
38.5	Siqueiros E	8.5399	-103.0106	17	112.96	Valley	No	Yes	Yes
39.1	Wilkes A	-9.0186	-109.2075	35	129.79	Valley	Yes	Yes	No
39.2	Wilkes B	-9.0622	-108.6880	74	129.74	Valley	Yes	Yes	No
40.1	Yaquina A	-6.2520	-107.2833	23	126.66	Valley	Yes	Yes	c.d.
40.2	Yaquina B	-6.1795	-106.9885	21	126.51	Valley	c.d.	Yes	c.d.
GORDA RIDGE									
41	Mendocino	40.3735	-126.0390	237	49.48	Ridge	Yes	No	No
JUAN DE FUCA RIDGE									
42.1	Blanco A	44.3327	-129.9170	94	51.06	Valley	Yes	Yes	No
42.2	Blanco B	44.0457	-129.2260	24	51.01	Valley	Yes	Yes	No
42.3	Blanco C	43.8909	-128.8385	41	50.99	Valley	Yes	Yes	No
42.4	Blanco D	43.3447	-127.5910	135	50.94	Ridge	Yes	Yes	Yes
42.5	Blanco E	43.0771	-126.8260	41	50.93	Valley	Yes	Yes	No
43 [†]	Sovanco	48.9763	-129.7650	135	53.90	Complex	No	No	No

Continued

TABLE 1 Structural Characterization of Global Oceanic Transform Faults—Cont'd

Fault # ^a	Name	Latitude	Longitude	Length (km)	Slip Rate (mm/yr)	Ridge/ Valley	Fracture Zones ^b	Abyssal Hills ^b	Transverse Ridges ^b
MID-ATLANTIC RIDGE									
44	15°20'	15.2762	−45.7372	193	23.57	Valley	Yes	Yes	No
45.1	Ascension A	−7.3741	−13.2457	58	29.54	Valley	Yes	Yes	No
45.2	Ascension B	−6.8837	−12.1360	203	29.51	Valley	Yes	Yes	No
46	Atlantis	30.0618	−42.3458	63	22.40	Valley	Yes	Yes	No
47.1	Bode Verde A	−12.2462	−14.5907	56	30.02	Valley	Yes	c.d.	No
47.2	Bode Verde B	−11.6761	−13.7003	162	29.98	Valley	Yes	c.d.	No
48	Chain	−1.2369	−14.5227	313	28.58	Valley	Yes	c.d.	No
49.1	Charlie Gibbs A	52.6168	−33.2600	203	21.73	Valley	Yes	c.d.	No
49.2	Charlie Gibbs B	52.1237	−30.8240	110	21.83	Valley	Yes	c.d.	No
50	Doldrums A	8.8229	−40.0169	109	25.56	Valley	Yes	c.d.	No
51	Doldrums B	8.2131	−38.7815	162	25.74	Valley	Yes	c.d.	No
52.1	Doldrums C	7.7201	−37.3782	149	25.89	Valley	Yes	c.d.	Yes
52.2	Doldrums D	7.4013	−35.6649	229	26.00	Valley	Yes	c.d.	Yes
52.3	Doldrums E	7.1946	−34.2776	77	26.08	Valley	Yes	c.d.	Yes
53	Falkland	−47.3095	−12.2515	181	27.44	Valley	Yes	c.d.	c.d.
54	Gough	−39.7910	−16.2299	56	28.98	Valley	Yes	c.d.	c.d.
55	Hayes	33.6636	−38.6474	80	21.65	Valley	Yes	Yes	No
56.1	Jan Mayen A	71.3311	−9.1831	127	15.45	Valley	Yes	c.d.	No
56.2	Jan Mayen B	71.1387	−7.3876	27	15.45	Valley	Yes	c.d.	No
57	Kane	23.7373	−45.6185	146	23.43	Valley	Yes	Yes	Yes
58	MAR 18S	−17.7210	−13.3749	91	30.34	Valley	Yes	c.d.	c.d.
59	MAR 21S	−21.2304	−11.7190	45	30.40	Valley	Yes	Yes	c.d.
60.1	MAR 22S A	−22.8158	−13.2588	85	30.39	Valley	Yes	c.d.	c.d.
60.2	MAR 22S B	−22.2763	−12.3656	86	30.40	Valley	Yes	c.d.	Yes
60.3	MAR 22S C	−22.0197	−11.8257	22	30.40	Valley	Yes	c.d.	Yes
61	MAR 25 50S	−25.6582	−13.7426	39	30.32	Valley	Yes	Yes	c.d.
62	MAR 25S	−24.8985	−13.5520	37	30.35	Valley	Yes	c.d.	c.d.
63	MAR 29 45S	−29.7608	−13.7662	27	30.10	Valley	Yes	Yes	c.d.
64.1	MAR 29S A	−29.1913	−13.4457	74	30.13	Valley	Yes	Yes	c.d.
64.2	MAR 29S B	−28.8651	−12.7703	59	30.15	Valley	Yes	Yes	c.d.

TABLE 1 Structural Characterization of Global Oceanic Transform Faults—Cont'd

Fault # ^a	Name	Latitude	Longitude	Length (km)	Slip Rate (mm/yr)	Ridge/Valley	Fracture Zones ^b	Abyssal Hills ^b	Transverse Ridges ^b
65.1	MAR 32S A	-32.4977	-14.4246	23	29.87	Valley	Yes	Yes	No
65.2	MAR 32S B	-32.2690	-13.9451	57	29.89	Valley	Yes	Yes	No
65.3	MAR 32S C	-32.1130	-13.4782	29	29.90	Valley	Yes	Yes	No
66	MAR 34S	-34.1605	-14.8348	69	29.71	Valley	Yes	Yes	No
67	MAR 35S	-35.3963	-16.5119	250	29.60	Valley	Yes	Yes	c.d.
68	MAR 40S	-40.3503	-16.6392	40	28.90	Valley	Yes	c.d.	c.d.
69	MAR 50S	-49.1266	-9.1361	110	26.90	Valley	Yes	No	Yes
70	MAR 5S	-5.0358	-11.9376	78	29.27	Valley	Yes	c.d.	c.d.
71	Marathon	12.6388	-44.4649	88	24.41	60/40	Yes	Yes	Yes
72	Oceanographer	35.1830	-35.6434	121	21.27	60/40	Yes	Yes	c.d.
73	Rio Grande	-28.2306	-12.9412	57	30.19	Valley	Yes	Yes	No
74	Romanche	-0.5279	-20.6298	878	28.27	Valley	Yes	c.d.	Yes
75.1	Saint Paul A	0.9335	-29.0195	297	27.71	Valley	Yes	c.d.	Yes
75.2	Saint Paul B	0.8731	-27.0355	146	27.77	Valley	Yes	c.d.	Yes
75.3	Saint Paul C	0.7399	-25.9188	96	27.83	Valley	Yes	c.d.	Yes
75.4	Saint Paul D	0.6166	-25.2346	50	27.88	Valley	Yes	c.d.	Yes
76	Strakhov	3.9423	-32.0787	108	26.96	Valley	Yes	Yes	No
77	Tetyaev	-16.2536	-13.7495	123	30.28	Valley	Yes	c.d.	c.d.
78	Vema	10.7778	-42.2864	307	24.98	Valley	Yes	Yes	Yes
PACIFIC ANTARCTIC RIDGE									
79	Heezen	-55.4170	-124.5340	382	79.02	Valley	Yes	Yes	Yes
80	Herron	-56.2889	-139.0725	26	75.45	Ridge	Yes	Yes	No
81.1	Hollister A	-54.2156	-136.9015	23	77.89	Valley	Yes	Yes	Yes
81.2	Hollister B	-54.3528	-136.2285	62	77.93	Valley	Yes	Yes	No
81.3	Hollister C	-54.5330	-135.3935	34	77.95	Valley	Yes	Yes	Yes
82	L'Astronome	-59.6459	-150.8520	56	68.94	Ridge	Yes	Yes	No
83	Le Geographe	-57.6251	-147.4950	70	71.90	Valley	Yes	Yes	No
84	Menard	-49.5637	-115.2415	208	85.47	Valley	Yes	Anomalous	Yes
85	PAR 161	-61.7789	161.5045	77	45.98	Valley	Yes	c.d.	c.d.
86	PAR 163	-62.0956	163.3585	85	46.71	Valley	Yes	c.d.	c.d.

Continued

TABLE 1 Structural Characterization of Global Oceanic Transform Faults—Cont'd

Fault # ^a	Name	Latitude	Longitude	Length (km)	Slip Rate (mm/yr)	Ridge/Valley	Fracture Zones ^b	Abyssal Hills ^b	Transverse Ridges ^b
87	PAR 165	−62.3835	165.4610	89	47.58	Valley	Yes	c.d.	c.d.
88	Pitman	−64.5321	−170.7790	71	56.74	Valley	Yes	Anomalous	Yes
89.1	Raitt A	−54.3331	−120.0970	88	80.94	Valley	Yes	Yes	Yes
89.2	Raitt B	−54.4874	−118.9355	58	80.99	Valley	Yes	Yes	No
90	Saint Exupery	−62.2439	−155.4175	42	64.73	Valley	Yes	Yes	c.d.
91	Tharp	−54.5941	−131.1230	462	78.82	Valley	Yes	Yes	Yes
92	Udintsev	−56.4114	−142.4340	325	74.49	Valley	Yes	Yes	Yes
93	Vacquier	−53.0360	−118.0905	52	82.29	Valley	Yes	Yes	c.d.
SOUTHEAST INDIAN RIDGE									
94.1	Amsterdam	−36.7018	78.6870	108	62.02	Valley	Yes	Yes	Yes
94.2	Boomerang	−37.3610	78.2141	35	62.15	Valley	No	Yes	No
95	Balleny	−61.4293	154.8090	350	64.50	60/40	Yes	c.d.	Yes
96	Birubi	−49.5044	127.2620	148	69.62	50/50	Yes	Yes	No
97	Euroka	−49.2295	126.0995	134	69.76	Valley	Yes	Yes	No
98	Geelvinck	−41.9641	84.7104	303	65.60	Valley	Yes	c.d.	Yes
99	George V A	−51.3519	139.7170	235	67.49	Valley	Yes	c.d.	c.d.
100	George V B	−53.2362	140.5525	179	67.30	Valley	Yes	c.d.	c.d.
101.1	Heemskerck A	−50.0051	115.5805	19	70.34	Valley	Yes	Yes	No
101.2	Heemskerck B	−49.8762	115.9340	24	70.34	Valley	Yes	Yes	No
101.3	Heemskerck C	−49.6495	116.1870	27	70.34	Valley	Yes	Yes	No
101.4	Heemskerck D	−49.3967	116.4695	31	70.33	Valley	Yes	Yes	No
102	Hillegoms Hole	−38.6621	78.3064	59	62.70	Valley	No	No	No
103	SEIR 100E	−47.6820	99.8058	129	69.46	Valley	Yes	Yes	Yes
104.1	SEIR 106E A	−49.0854	106.2620	56	70.11	Valley	Yes	Yes	No
104.2	SEIR 106E B	−48.6360	106.7910	59	70.12	Valley	Yes	Yes	No
105	SEIR 120	−49.4884	120.4165	154	70.19	Valley	Yes	c.d.	c.d.
106	SEIR 121	−49.3559	121.5315	80	70.13	Valley	Yes	c.d.	c.d.
107.1	SEIR 122	−49.7086	122.7255	50	70.04	Valley	No	No	No
107.2	Warringa A	−49.4070	123.3800	38	70.00	Valley	Yes	c.d.	c.d.
107.3	Warringa B	−49.0728	123.8695	49	69.97	Valley	Yes	c.d.	c.d.

TABLE 1 Structural Characterization of Global Oceanic Transform Faults—Cont'd

Fault # ^a	Name	Latitude	Longitude	Length (km)	Slip Rate (mm/yr)	Ridge/Valley	Fracture Zones ^b	Abyssal Hills ^b	Transverse Ridges ^b
108	SEIR 88E	-41.9219	88.4153	65	66.47	Valley	Yes	Yes	c.d.
109	SEIR 96E A	-45.6635	96.0315	89	68.69	Ridge	Yes	No	Yes
110	SEIR 96E B	-46.4296	96.1364	40	68.82	Valley	Yes	No	No
111	St Vincent	-54.4960	144.1215	58	66.50	Valley	Yes	c.d.	c.d.
112.1	Tasman A	-55.2315	146.3335	90	66.05	Ridge	Yes	c.d.	c.d.
112.2	Tasman B	-56.5921	147.2790	218	65.82	Valley	Yes	c.d.	c.d.
112.3	Tasman C	-57.7873	148.4671	62	65.51	Valley	Yes	c.d.	c.d.
112.4	Tasman D	-58.8662	149.2500	173	65.29	Valley	Yes	c.d.	Yes
112.5	Tasman E	-59.8753	150.5617	82	65.29	Valley	Yes	c.d.	c.d.
113	Ter Tholen	-33.4444	77.7178	89	60.26	Valley	Yes	Yes	Yes
114	Vlamingh	-41.4712	80.3625	123	64.35	60/40	Yes	Yes	Yes
115.1	Zeehaen A	-50.2303	114.0686	31	70.35	Valley	Yes	Yes	No
115.2	Zeehaen B	-49.9722	114.2949	31	70.35	Valley	Yes	Yes	No
116.1	Zeewolf A	-35.4438	78.4580	32	61.41	Valley	Yes	Yes	No
116.2	Zeewolf B	-35.1800	78.6366	29	61.36	Valley	Yes	Yes	No
SOUTH SCOTIA RIDGE									
117	Shakleton	-59.1128	-59.7490	332	6.83	60/40	Yes	No	No
SOUTHWEST INDIAN RIDGE									
118.1	Andrew Bain A	-47.4907	32.2321	87	13.35	Valley	Yes	Yes	Yes
118.2	Andrew Bain B	-50.4204	29.6504	148	13.34	Valley	Yes	Yes	Yes
118.3	Andrew Bain C	-50.9500	29.0100	471	13.33	Valley	Yes	Yes	Yes
119	Atlantis II	-32.7572	57.0414	201	12.02	Valley	Yes	Yes	Yes
120	Bouvet	-54.2649	1.9220	201	12.72	Valley	Yes	No	No
121.1	Discovery II A	-43.2960	41.6629	124	12.91	Valley	Yes	c.d.	Yes
121.2	Discovery II B	-41.8592	42.5948	216	12.89	Valley	Yes	c.d.	Yes
122	Du Toit	-53.0075	25.4810	130	13.29	Valley	Yes	Yes	No
123	Eric Simpson	-43.7349	39.2474	89	13.03	Valley	Yes	c.d.	c.d.
124	Gallieni	-36.6370	52.3209	114	12.34	Valley	Yes	c.d.	Yes
125	Gauss	-34.9983	54.1242	59	12.23	Valley	Yes	c.d.	c.d.
126	Gazelle	-35.8023	53.4257	81	12.27	Valley	Yes	c.d.	c.d.

Continued

TABLE 1 Structural Characterization of Global Oceanic Transform Faults—Cont'd

Fault # ^a	Name	Latitude	Longitude	Length (km)	Slip Rate (mm/yr)	Ridge/Valley	Fracture Zones ^b	Abyssal Hills ^b	Transverse Ridges ^b
127	Indomed	−39.4741	46.1057	141	12.73	Valley	Yes	c.d.	c.d.
128	Islas Orcadas	−54.1828	6.0992	100	12.85	Valley	Yes	c.d.	c.d.
129	Marion	−46.4684	33.6623	109	13.22	Valley	Yes	Yes	c.d.
130	Melville	−29.8412	60.7767	92	11.74	60/40	Yes	Yes	Yes
131	Novara	−31.4254	58.4107	45	11.93	Valley	Yes	c.d.	c.d.
132	Prince Edward	−45.4457	35.1282	146	13.19	Valley	Yes	Yes	Yes
133	Shaka	−53.5524	9.0237	199	12.92	Valley	Yes	No	Yes

^a Fault segments with the same base number are part of the same segmented RTF system.

^b c.d. stands for cannot distinguish, the resolution of the data was not sufficient.

[†] Sovanco is neither a throughgoing ridge or valley, but rather a series of rotated crustal blocks (see Cowan et al., 1986).

accommodated. The length of the fracture zone, combined with a known slip rate, can be used to infer the age of the fault. A lack of fracture zones may indicate a young, evolving fault, as in the case of the Discovery Transform Fault on the EPR (Wolfson-Schwehr et al., 2014), or a fault that is undergoing reorganization. Fracture zones are also markers of past changes in plate motion, as the ever-growing seam preserves the change in the rock record.

Abyssal hill fabric, bands of topographic highs that trend approximately parallel to the MOR axis, cover much of the seafloor, except where buried by sediment (Dietz et al., 1954; Menard and Atwater, 1968; Searle, 1984). The orientation of abyssal hill fabric typically changes as it reaches the RTI, and begins to curve into the transform fault (Lonsdale, 1978; Fox and Gallo, 1984; Fornari et al., 1989), reflecting the change in the stress regime from a primarily ridge-normal extensional stress to a transform parallel shear stress (Sonder and Pockalny, 1999; Croon et al., 2010). The curve of the abyssal hill fabric follows that of the ridge into the transform domain, such that on the left-lateral faults the abyssal hills form the shape of the letter “J.” Sonder and Pockalny (1999) and Croon et al. (2010) noted the presence of “anomalously rotated” abyssal hills along the Clipperton Transform Fault on the EPR, as well as along the Menard and Pitman Transform Faults, both on the Pacific-Antarctic Ridge. The studies suggest that anomalously rotated abyssal hills, which appear to stay straight as they approach the transform, or are slightly rotated toward the RTI, form during periods of increased compression along the fault, which leads to distributed strike-slip deformation away from the fault and the deflection of abyssal-hill fabric.

Transverse ridges are topographic highs that run parallel to the fracture zones on some oceanic transform faults. They may extend from the transform domain, past the RTI, and continue for 100s of kilometers. Transverse ridges are thought to form as a flexural response of the lithosphere when changes in the plate motion cause fracture-zone normal extension. Under such extension, normal faulting causes uplift on the older side of the fracture zone, resulting in ridge formation, and downwarping on the younger side, forming anomalously deep basins (Pockalny et al., 1996). This proposed method of formation predicts that transverse ridges will preferentially form along fracture-zone extensions that accompany faults that have undergone past periods of transpression (Fig. 2).

Of the 204 individual fault segments delineated in this characterization (Table 1), 188 have discernable fracture zones. Normal abyssal hill fabric is observed along 116 individual fault segments, while anomalous abyssal hill fabric is apparent along only 3 faults. Nine fault segments have median ridges, 188 have median valleys, and 7 displayed a mixture of median ridge and valley. Transverse ridges are observed along 55 fault segments. In many instances, the data around the transform fault was too coarse to determine the presence or absence of features.

3 UPDATED GLOBAL CHARACTERIZATION OF OCEANIC TRANSFORM FAULT SEISMICITY

The scaling relations of Boettcher and Jordan (2004) were updated with fault lengths and slip rates from our global characterization of oceanic transform fault structure described above, as well as ~ 16 additional years of seismic data. We applied the scaling relations to ridge-transform faults only, excluding some oceanic transform faults in the global characterization on the basis that one or both endpoints did not terminate in a RTI (e.g., the Mendocino Transform Fault, where the eastern end forms the Gorda-Pacific-North American plate triple junction). The decision of whether to analyze adjacent fault segments as a single through-going fault or as individual fault segments was based on the critical step-over length, L_S (Eq. 2). Wolfson-Schwehr et al. (2017) found that step-overs greater than or equal to L_S thin the lithosphere beneath the step-over, significantly reducing in the seismogenic area of the combined fault segments. Therefore, in our scaling relation analysis, we treated adjacent fault segments as two individual faults if the step-over between them is longer than L_S , and as a single, through-going fault if the step-over between them is shorter than L_S . In all, only three pairs of adjacent segments have adjoining step-overs less than L_S : Andrew Bain segments A and B, Blanco segments C and D, and Jan Mayen segments A and B. Thus, most of the segments we identified were treated as individual faults in our scaling analysis described below.

We followed Boettcher and Jordan (2004) and only included RTFs in our analysis if $L \geq 75$ km, A_T , with a base isotherm of 600°C , ≥ 350 km², and there was at least one earthquake above the catalog completeness magnitude of 5.6. Of the 204 individual fault segments in our global characterization, 198 met the requirements of being ridge-bounded fault segments (RTFs), with 85 of those segments meeting the additional L , A_T , and magnitude requirements. The length and area requirements eliminate small faults where a large portion of the seismicity may be attributed to normal faulting along the MOR or poorly located earthquakes that occurred on an adjacent RTF segment. The uncertainty in earthquake locations from the CMT catalog is of the order of 50 km for RTFs (Ekström et al., 2012; Wolfson-Schwehr et al., 2014). For each RTF segment that meets the L and A_T requirements, a bounding polygon was used to select the earthquakes to associate with each fault from a 41-year seismic record obtained from the CMT catalog (Ekström et al., 2012), from January 1, 1976 through December 31, 2016. Initial bounds for the polygons were set to 100 km on the fault-parallel sides, and 50 km on the ridge-parallel sides. These bounds were then reduced as necessary to avoid overlap with the bounding polygons of neighboring faults.

Earthquakes on RTFs have been observed to follow a tapered Gutenberg-Richter distribution (Kagan and Jackson, 2000; Bird et al., 2002; Boettcher and Jordan, 2004):

$$N(M) = N_0 \left(\frac{M_0}{M} \right)^\beta \exp \left(\frac{M_0 - M}{M_C} \right) \quad (3)$$

where $N(M)$ is the cumulative number of events with a seismic moment greater than, or equal to, M , N_0 is the cumulative number of events above the completeness threshold moment, M_0 , and β is the slope of the distribution below the exponential roll-off at M_C , the largest expected earthquake on the fault. To ensure there were enough earthquakes to allow for statistically robust computations, the RTFs were divided into four groups based on A_T . Thermal area divisions were chosen such that each of the four groups had roughly the same number of events over the catalog completeness level. The scaling parameters were then estimated by fitting Eq. (3) to the groups using a maximum likelihood approach (Boettcher and Jordan, 2004). Event frequencies for each group were binned by 0.1 increments of $\log(M)$, and \bar{n}_k , the number of events in each group, was assumed to be Poisson-distributed with an expected value, $n_k \approx -\Delta M_k dN(M_k)/dM$, where $N(M_k)$ is the cumulative number of events in each group with a seismic moment $\geq M_k$. The log likelihood function then computes a best fit β and M_C value for each A_T group:

$$\begin{aligned} Lik(\beta M_C) = \sum_k \left\{ \ln \left[n_k N_0 \left(\frac{\beta}{M_k} + \frac{1}{M_C} \right) \left[\frac{M_k}{M_0} \right]^{-\beta} \cdot \exp \left[\frac{M_0 - M_k}{M_C} \right] \right] \right. \\ \left. - N_0 \left(\frac{\beta}{M_k} + \frac{1}{M_C} \right) \left[\frac{M_k}{M_0} \right]^{-\beta} \cdot \exp \left[\frac{M_0 - M_k}{M_C} \right] - \ln(n_k!) \right\} \end{aligned} \quad (4)$$

The 95% confidence region for the M_C estimate obtained for each group of faults includes the maximum likelihood estimate obtained with β fixed at two-thirds. These results agree with the maximum likelihood scaling of Bird et al. (2002) and Boettcher and Jordan (2004), who showed that RTFs show self-similar scaling below the upper cutoff moment. The maximum likelihood estimates of M_C , with β fixed at two-thirds, were then used to compute scaling relations for the effective seismogenic area of the fault, A_E , the area displaced by the observed moment release rate per unit tectonic slip; and A_C , the area of the fault ruptured in the largest expected earthquake. The equations for A_E and A_C follow Boettcher and Jordan (2004):

$$A_E = \left(\frac{\sum M}{\mu VT} \right) \rightarrow C_E A_T^\alpha = C_E C_T L^{3/2} V^{-1/2} \quad (5)$$

$$A_C = \left(\frac{M_C}{\Delta \sigma} \right)^{2/3} \rightarrow C_{AC} A_T^\gamma = C_{AC} C_T L^{3/4} V^{-1/4} \quad (6)$$

where μ , the shear modulus, is 44.1 GPa, the lower crustal value from the preliminary reference Earth model (PREM) (Dziewonski and Anderson, 1981), T is the time period of the seismic catalog, and $\Delta \sigma$ is the static stress drop (fixed at 3 MPa). The scaling exponents, α and γ , were derived according to Eqs. (5) and (6), respectively. Our best-fit value for α is 1.0, such that A_E is directly proportional to A_T , as was found previously by Boettcher and

Jordan (2004). Our best-fit value for γ is 0.34, which is within the 95% confidence limits found by Boettcher and Jordan (2004).

For A_E , the constant C_E is directly related to χ , the seismic coupling coefficient. In our current analysis, χ increased from the original value in Boettcher and Jordan (2004) of ~ 0.15 to ~ 0.22 , indicating that more of the motion along RTFs is accommodated by seismicity when segmentation is considered. For A_C , the reduction in γ from 0.5 (Boettcher and Jordan, 2004) to 0.34 suggests a lesser dependence on the seismogenic area of the fault, and consequently on the fault parameters length and slip rate. The constant C_{AC} in our current analysis increased from an original value of $3.2 \times 10^3 \text{ km}$ to a value of $2.0 \times 10^5 \text{ km}^{(4/3)}$ (the change in units from km to $\text{km}^{(4/3)}$ is related to the decrease in γ from 0.5 to $1/3$). This increase indicates that the largest expected earthquakes on the fault (M_C) rupture a larger portion of the fault area when segmentation is considered. Breaking segmented fault systems into individual faults associates more of the observed earthquakes with small faults. Therefore, the observed increases in both A_E and A_C compared to Boettcher and Jordan (2004) are expected. Table 2 presents the predicted values of χ and M_C computed from our updated scaling relations for the individual fault segments used in this analysis.

The value of C_{AC} is also dependent on the constant stress drop model assumed in the computation of A_C , with stress-drop set at 3 MPa, as was done in Boettcher and Jordan (2004). Estimates of stress drops for RTF earthquakes are few and far between, as they necessitate high-quality waveform analysis or knowing the rupture dimensions, usually inferred from after-shock sequences. Computed stress drops for an event on the Blanco Transform Fault, where aftershocks were delineated using SOSUS T-phase data, and for a few events on the Romanche Transform Fault, where dimension was obtained from teleseismic waveform inversions, suggest that RTF stress drops may be $< 1 \text{ MPa}$ (Boettcher and Jordan, 2004). Moyer et al. (2017) performed spectral analysis on ocean bottom seismic data and found stress drops of 0.04–4 MPa for moderate-sized earthquakes on Gofar Transform Fault. Boettcher and McGuire (2009) computed a range of estimated stress drops for RTFs by comparing estimated recurrence times for the largest observed earthquakes to the actual observed recurrence times and estimated RTF stress drops in the range of 3–10 MPa. In our scaling analysis, stress drop is taken to be 3 MPa. For some faults, this value may be too high, in which case the computed A_C , as well as the value of C_{AC} , would be too low (Eq. 6).

4 THE EFFECT OF FAULT STRUCTURE ON THE SEISMICITY

Combining the global characterization of oceanic transform fault structure with an updated scaling analysis allows us to observe how structure may affect observed seismic behavior on RTFs. Specifically, we tested two basic hypotheses: (1) that average seismic coupling would increase when segmentation was accounted for (e.g., Gregg et al., 2006) and (2) that physical segmentation of RTFs is the reason why the largest RTF earthquakes don't rupture the full fault area. If segmentation were the primary explanation, then the new scaling relations for A_E and A_C would have scaling constants and exponents near unity; i.e., the majority of the faults in Fig. 5 would line up on the 1:1 lines. However, this is not the case, thus segmentation alone can explain neither the seismic deficit nor the smaller than the predicted

TABLE 2 Predicted and Observed Seismicity on Mid-Ocean Ridge Transform Faults

Fault Segment #	Name	Latitude	Longitude	Length (km)	Slip Rate (mm/yr)	Max M_W	Max M_W exp.	χ	Width (km)	A_T (km ²)	A_E (km ²)	A_E pred. (km ²)	A_C (km ²)	A_C pred. (km ²)
AMERICA ANTARCTIC RIDGE														
1	Bullard A	−59.1299	−17.1358	95	12.99	6.2	6.4	0.24	11.1	1052	249	235	86	143
2	Bullard B	−58.1845	−11.4861	526	13.43	6.8	7.0	0.19	25.6	13,479	2585	3018	331	512
3	Conrad	−55.7107	−3.1638	198	14.51	6.7	6.6	0.32	15.1	2995	963	670	290	241
ADEN RIDGE														
4	Alula Fartak	13.9416	51.7064	203	18.90	6.6	6.6	0.20	13.4	2724	543	610	233	230
5	Owen	11.4232	57.5424	335	22.84	6.5	6.8	0.15	15.7	5254	777	1176	163	320
CHILE RISE														
6	Challenger A	−36.9977	−96.6218	78	46.56	5.8	6.2	0.04	5.3	414	17	93	32	90
7	Challenger B ^a	−37.1051	−95.7193	67	46.58	–	6.2	–	4.9	329	–	74	–	80
8	Challenger C ^a	−37.2455	−95.1854	20	46.61	–	5.8	–	2.7	53	–	12	–	32
9	Challenger D ^a	−37.3206	−94.5776	82	46.62	5.4	6.2	0.02	5.4	446	8	100	14	93
10	Chile 38S A ^a	−38.3337	−93.6255	43	46.85	5.3	6.0	0.02	3.9	169	4	38	12	57
11	Chile 38S B ^a	−38.4119	−92.9817	68	46.86	–	6.2	–	4.9	336	–	75	–	81
12	Chile 39S	−38.9649	−92.0683	84	46.98	6.1	6.2	0.16	5.5	460	74	103	70	95
13	Chile A	−35.1408	−106.5120	493	46.42	6.3	6.8	0.05	13.3	6580	352	1473	112	358
14	Chile B	−35.8981	−102.7915	186	46.46	6.7	6.5	0.31	8.2	1525	474	341	297	172
15	Chile C	−36.2066	−99.4233	420	46.43	6.5	6.8	0.14	12.3	5174	729	1158	174	317
16	Chiloe ^a	−43.0261	−83.0813	61	47.82	5.6	6.1	0.08	4.7	282	22	63	21	74
17	Darwin ^a	−45.8952	−76.3639	53	48.30	5.9	6.1	0.20	4.3	227	45	51	41	66
18	Guafo	−44.6952	−80.1486	286	48.10	6.4	6.6	0.16	10.0	2857	447	640	157	236

19	Guamblin	−45.7052	−77.3701	80	48.27	6.0	6.2	0.09	5.3	422	37	94	61	91
20	Valdavia A ^a	−41.0899	−91.5642	49	47.42	5.4	6.1	0.03	4.2	204	6	46	15	63
21	Valdavia B	−41.1975	−90.8074	77	47.45	5.8	6.2	0.07	5.2	402	29	90	33	88
22	Valdavia C	−41.3049	−89.7437	97	47.47	5.7	6.3	0.03	5.9	568	19	127	29	105
23	Valdavia D	−41.3474	−88.4437	119	47.48	5.7	6.3	0.03	6.5	772	24	173	29	123
24	Valdavia E	−41.4080	−86.7164	165	47.51	5.9	6.4	0.04	7.6	1260	55	282	45	157
25	Valdavia F ^a	−41.4853	−85.1446	69	47.54	5.6	6.2	0.02	4.9	341	7	76	21	81
26	Valdavia G ^a	−41.5714	−84.5249	23	47.56	–	5.8	–	2.8	65	–	15	–	36

CENTRAL INDIAN RIDGE

27	Argo	−13.5851	66.3508	102	33.33	6.0	6.3	0.13	7.2	731	95	164	54	119
28	CIR 10S ^a	−10.0862	66.5586	76	30.95	5.0	6.2	0.00	6.4	488	1	109	5	97
29	CIR 12 12	−11.8548	65.9932	106	31.90	5.7	6.3	0.03	7.5	791	24	177	26	124
30	CIR 16S	−16.2924	66.9738	110	35.58	5.6	6.3	0.04	7.2	792	31	177	21	124
31	CIR 1S ^a	−1.1861	67.5232	50	29.87	5.8	6.1	0.19	5.3	265	51	59	35	72
32	CIR 5S ^a	−4.7309	68.5886	49	31.00	5.3	6.1	0.04	5.1	252	9	56	12	70
33	CIR 6S ^a	−6.8331	68.2378	89	31.35	5.4	6.3	0.01	6.9	614	4	137	15	109
34	CIR 7S ^a	−7.6133	68.0794	62	30.17	5.4	6.2	0.02	5.9	364	6	81	15	84
35	Egeria ^a	−20.1347	66.5795	46	38.13	5.5	6.1	0.08	4.5	207	16	46	17	63
36	Flinders ^a	−20.2447	67.2598	65	38.48	5.2	6.2	0.03	5.3	346	9	77	10	82
37	Gemino ^a	−22.7804	69.2857	38	40.99	5.4	6.0	0.06	4.0	150	10	34	14	54
38	Mabahiss ^a	−3.0415	68.1212	42	30.48	5.6	6.0	0.05	4.8	202	11	45	24	63
39	Marie Celeste	−17.5098	66.0021	219	35.99	6.6	6.6	0.47	10.1	2213	1034	495	232	207

Continued

TABLE 2 Predicted and Observed Seismicity on Mid-Ocean Ridge TransformFaults—Cont'd

Fault Segment #	Name	Latitude	Longitude	Length (km)	Slip Rate (mm/yr)	Max M_W	Max M_W exp.	χ	Width (km)	A_T (km ²)	A_E (km ²)	A_E pred. (km ²)	A_C (km ²)	A_C pred. (km ²)
40	Sealark ^a	−3.8789	68.4740	63	30.78	5.1	6.2	0.00	5.9	369	1	83	7	85
41	Vema II	−8.9231	67.4427	237	30.63	6.2	6.6	0.06	11.4	2700	158	604	81	229
42	Vityaz	−5.6877	68.3685	105	31.14	5.7	6.3	0.02	7.5	790	13	177	25	124
EAST PACIFIC RISE														
44	Discovery A ^a	−4.0067	−104.3510	36	123.55	6.0	5.8	0.47	2.2	80	38	18	56	40
45	Discovery B ^a	−3.9981	−104.0080	27	123.48	5.8	5.8	0.30	1.9	52	16	12	32	32
46	Garrett A ^a	−13.4112	−112.1545	39	133.99	5.9	5.9	0.13	2.2	87	12	19	42	41
47	Garrett B ^a	−13.4240	−111.8215	26	133.94	5.2	5.7	0.02	1.8	47	1	11	10	30
48	Garrett C ^a	−13.4496	−111.5255	32	133.90	5.7	5.8	0.07	2.0	65	5	14	30	35
49	Garrett D ^a	−13.4760	−111.2430	27	133.86	5.8	5.7	0.27	1.9	50	13	11	32	31
50	GoC 24N A ^a	24.2430	−109.0481	61	50.37	6.1	6.1	0.13	4.5	275	37	62	71	73
51	GoC 24N B ^a	23.7697	−108.5794	63	50.37	6.1	6.1	0.26	4.6	289	75	65	76	75
52	GoC 25N	24.9837	−109.5170	119	49.85	6.7	6.3	0.50	6.3	753	376	169	268	121
53	Gofar A	−4.5939	−105.8490	95	124.55	6.2	6.2	0.24	3.6	341	81	76	86	81
54	Gofar B ^a	−4.5792	−105.2640	29	124.40	6.0	5.8	0.30	2.0	58	17	13	62	34
55	Gofar C ^a	−4.5562	−104.8820	46	124.30	6.1	5.9	0.38	2.5	115	44	26	64	47
56	Orozco A ^a	15.4137	−105.1145	46	87.81	5.3	6.0	0.02	2.9	137	2	31	10	52
57	Orozco B ^a	15.1573	−104.5815	23	88.85	5.6	5.7	0.09	2.1	48	4	11	23	31
58	Quebrada A ^a	−3.7447	−103.6830	27	123.12	5.6	5.8	0.07	2.0	52	4	12	24	32
59	Quebrada B ^a	−3.7325	−103.4445	22	123.05	5.3	5.7	0.02	1.7	38	1	9	11	27

60	Quebrada C ^a	−3.7005	−103.1895	27	122.97	4.9	5.8	0.00	1.9	52	0	12	4	32
61	Quebrada D ^a	−3.7302	−102.8605	42	122.94	5.6	5.9	0.04	2.4	101	4	23	20	44
62	Rivera A	19.5693	−108.6785	177	73.00	6.3	6.4	0.12	6.4	1130	136	253	125	148
63	Rivera B	18.7629	−107.1555	197	73.00	6.9	6.5	0.45	6.7	1326	594	297	442	161
64	Siqueiros A ^a	8.3925	−104.0053	24	112.24	5.5	5.7	0.10	1.9	46	4	10	18	30
65	Siqueiros B ^a	8.4404	−103.6818	34	112.48	5.6	5.8	0.02	2.3	77	2	17	20	39
66	Siqueiros C ^a	8.4805	−103.4112	18	112.68	5.8	5.6	0.68	1.7	30	20	7	32	24
67	Siqueiros D ^a	8.5105	−103.2089	17	112.89	5.8	5.6	0.57	1.6	27	16	6	35	23
68	Siqueiros E ^a	8.5399	−103.0106	17	112.96	5.9	5.6	0.52	1.6	27	14	6	43	23
69	Tomayo ^a	23.0780	−108.3355	65	50.95	6.5	6.1	0.34	4.6	301	102	67	163	76
70	Wilkes A ^a	−9.0186	−109.2075	35	129.79	5.9	5.8	0.27	2.2	75	20	17	42	38
71	Wilkes B ^a	−9.0622	−108.6880	74	129.74	6.1	6.1	0.11	3.1	230	25	52	63	67
72	Yaquina A ^a	−6.2520	−107.2833	23	126.66	5.6	5.7	0.19	1.7	41	8	9	21	28
73	Yaquina B ^a	−6.1795	−106.9885	21	126.51	5.2	5.7	0.04	1.7	35	1	8	9	26

JUAN DE FUCA RIDGE

74	Blanco A	44.3327	−129.9170	94	51.06	6.2	6.3	0.16	5.5	523	86	117	88	101
75	Blanco B ^a	44.0457	−129.2260	24	51.01	6.2	5.8	0.57	2.8	67	38	15	91	36
76	Blanco C ^a	43.8909	−128.8385	41	50.99	5.4	6.0	0.01	3.7	151	2	34	16	54
77	Blanco D & E	43.3447	−127.5910	178	50.94	6.4	6.5	0.23	7.7	1363	312	305	149	163
78	Sovanco	48.9763	−129.7650	135	53.90	6.7	6.4	0.58	6.5	876	508	196	280	130

Continued

TABLE 2 Predicted and Observed Seismicity on Mid-Ocean Ridge TransformFaults—Cont'd

Fault Segment #	Name	Latitude	Longitude	Length (km)	Slip Rate (mm/yr)	Max M_W	Max M_W exp.	χ	Width (km)	A_T (km ²)	A_E (km ²)	A_E pred. (km ²)	A_C (km ²)	A_C pred. (km ²)
<i>MID-ATLANTIC RIDGE</i>														
79	15 20	15.2762	−45.7372	193	23.57	6.0	6.6	0.04	11.7	2262	81	506	55	210
80	Ascension A ^a	−7.3741	−13.2457	58	29.54	5.6	6.2	0.03	5.8	333	9	74	22	80
81	Ascension B	−6.8837	−12.1360	203	29.51	6.0	6.6	0.05	10.7	2180	110	488	53	206
82	Atlantis	30.0618	−42.3458	63	22.40	5.8	6.2	0.06	6.9	432	26	97	32	92
83	Bode Verde A ^a	−12.2462	−14.5907	56	30.02	4.9	6.1	0.00	5.6	313	0	70	4	78
84	Bode Verde B ^a	−11.6761	−13.7003	162	29.98	6.2	6.5	0.07	9.5	1542	107	345	93	173
85	Chain	−1.2369	−14.5227	313	28.58	6.8	6.7	0.33	13.6	4242	1380	950	355	287
86	Charlie Gibbs A	52.6168	−33.2600	203	21.73	7.1	6.6	0.69	12.5	2541	1742	569	665	222
87	Charlie Gibbs B	52.1237	−30.8240	110	21.83	5.8	6.4	0.03	9.2	1011	30	226	33	140
88	Doldrums A	8.8229	−40.0169	109	25.56	5.6	6.4	0.02	8.5	922	14	206	24	134
89	Doldrums B	8.2131	−38.7815	162	25.74	7.0	6.5	0.82	10.3	1664	1367	373	566	180
90	Doldrums C	7.7201	−37.3782	149	25.89	6.2	6.5	0.07	9.8	1464	104	328	79	169
91	Doldrums D	7.4013	−35.6649	229	26.00	6.5	6.6	0.09	12.1	2783	248	623	166	233
92	Doldrums E	7.1946	−34.2776	77	26.08	5.9	6.3	0.16	7.0	542	87	121	43	103
93	Falkland	−47.3095	−12.2515	181	27.44	6.0	6.5	0.04	10.5	1904	73	426	58	192
94	Gough ^a	−39.7910	−16.2299	56	28.98	4.9	6.1	0.00	5.7	319	0	71	4	79
95	Hayes	33.6636	−38.6474	80	21.65	6.1	6.3	0.16	7.8	630	99	141	71	111
96	Jan Mayen A & B	71.3311	−9.1831	161	15.45	6.7	6.6	0.43	13.2	2128	923	476	310	203
97	Kane	23.7373	−45.6185	146	23.43	6.4	6.5	0.21	10.2	1492	314	334	147	170

98	MAR 18S ^a	−17.7210	−13.3749	91	30.34	5.5	6.3	0.04	7.1	645	24	145	17	112
99	MAR 21S ^a	−21.2304	−11.7190	45	30.40	–	6.1	–	4.9	224	–	50	–	66
100	MAR 22S A ^a	−22.8158	−13.2588	85	30.39	5.4	6.3	0.01	6.8	582	8	130	13	106
101	MAR 22S B ^a	−22.2763	−12.3656	86	30.40	5.2	6.3	0.01	6.9	592	3	133	9	107
102	MAR 22S C ^a	−22.0197	−11.8257	22	30.40	5.2	5.8	0.02	3.5	76	2	17	9	39
103	MAR 25 50S ^a	−25.6582	−13.7426	39	30.32	5.5	6.0	0.11	4.6	181	20	41	17	59
104	MAR 25S ^a	−24.8985	−13.5520	37	30.35	5.4	6.0	0.04	4.5	167	6	37	14	57
105	MAR 29 45S ^a	−29.7608	−13.7662	27	30.10	–	5.9	–	3.9	104		23	–	45
106	MAR 29S A ^a	−29.1913	−13.4457	74	30.13	5.0	6.2	0.00	6.5	475	1	106	5	96
107	MAR 29S B ^a	−28.8651	−12.7703	59	30.15	5.2	6.2	0.01	5.7	338	4	76	8	81
108	MAR 32S A ^a	−32.4977	−14.4246	23	29.87	–	5.9	–	3.6	82	–	18	–	40
109	MAR 32S B ^a	−32.2690	−13.9451	57	29.89	5.3	6.1	0.01	5.6	322	4	72	11	79
110	MAR 32S C ^a	−32.1130	−13.4782	29	29.90	5.9	5.9	0.19	4.1	117	22	26	40	48
111	MAR 34S ^a	−34.1605	−14.8348	69	29.71	5.2	6.2	0.02	6.3	431	9	96	8	92
112	MAR 35S	−35.3963	−16.5119	250	29.60	6.9	6.6	0.50	11.9	2975	1500	666	459	241
113	MAR 40S ^a	−40.3503	−16.6392	40	28.90	–	6.0	–	4.9	193	–	43	–	61
114	MAR 50S	−49.1266	−9.1361	110	26.90	5.4	6.4	0.01	8.2	911	6	204	15	133
115	MAR 55 ^a	−5.0358	−11.9376	78	29.27	5.6	6.3	0.01	6.7	521	8	117	24	101
116	Marathon	12.6388	−44.4649	88	24.41	5.5	6.3	0.02	7.8	684	15	153	19	115
117	Oceanographer	35.1830	−35.6434	121	21.27	6.3	6.4	0.42	9.8	1182	498	265	111	152
118	Rio Grande ^a	−28.2306	−12.9412	57	30.19	5.2	6.1	0.02	5.6	321	5	72	10	79
119	Romanche	−0.5279	−20.6298	878	28.27	7.1	7.0	0.31	22.8	20,036	6208	4485	717	624

Continued

TABLE 2 Predicted and Observed Seismicity on Mid-Ocean Ridge TransformFaults—Cont'd

Fault Segment #	Name	Latitude	Longitude	Length (km)	Slip Rate (mm/yr)	Max M_W	Max M_W exp.	χ	Width (km)	A_T (km ²)	A_E (km ²)	A_E pred. (km ²)	A_C (km ²)	A_C pred. (km ²)
120	Saint Paul A	0.9335	−29.0195	297	27.71	6.6	6.7	0.21	13.4	3982	829	891	237	278
121	Saint Paul B	0.8731	−27.0355	146	27.77	5.9	6.5	0.07	9.4	1371	90	307	43	163
122	Saint Paul C	0.7399	−25.9188	96	27.83	6.1	6.3	0.23	7.6	730	167	163	66	119
123	Saint Paul D ^a	0.6166	−25.2346	50	27.88	6.0	6.1	0.12	5.5	274	33	61	54	73
124	Strakhov ^a	3.9423	−32.0787	108	26.96	5.5	6.4	0.02	8.2	885	18	198	17	131
125	Tetyaev ^a	−16.2536	−13.7495	123	30.28	5.5	6.4	0.01	8.2	1015	8	227	19	141
126	Vema	10.7778	−42.2864	307	24.98	6.9	6.7	0.48	14.4	4407	2113	987	485	293
PACIFIC ANTARCTIC RIDGE														
127	Heezen	−55.4170	−124.5340	382	79.02	6.4	6.7	0.11	9.0	3441	389	770	139	259
128	Herron ^a	−56.2889	−139.0725	26	75.45	5.9	5.8	0.27	2.4	63	17	14	44	35
129	Hollister A ^a	−54.2156	−136.9015	23	77.89	6.3	5.8	0.55	2.2	51	29	12	106	32
130	Hollister B ^a	−54.3528	−136.2285	62	77.93	6.4	6.1	0.59	3.7	227	133	51	148	66
131	Hollister C ^a	−54.5330	−135.3935	34	77.95	6.1	5.9	0.57	2.7	92	52	21	76	42
132	L'Astronome ^a	−59.6459	−150.8520	56	68.94	6.0	6.1	0.18	3.7	207	37	46	53	63
133	Le Geographe ^a	−57.6251	−147.4950	70	71.90	5.9	6.1	0.10	4.0	283	28	63	50	74
134	Menard	−49.5637	−115.2415	208	85.47	6.4	6.5	0.18	6.4	1330	245	298	143	161
135	PAR 161	−61.7789	161.5045	77	45.98	6.0	6.2	0.19	5.3	408	78	91	55	89
136	PAR 163 ^a	−62.0956	163.3585	85	46.71	5.3	6.2	0.01	5.5	470	3	105	12	96
137	PAR 165	−62.3835	165.4610	89	47.58	5.9	6.2	0.15	5.6	499	74	112	46	98
138	Pitman ^a	−64.5321	−170.7790	71	56.74	5.3	6.2	0.00	4.6	326	1	73	11	80

139	Raitt A ^a	−54.3331	−120.0970	88	80.94	5.4	6.2	0.01	4.3	376	3	84	13	86
140	Raitt B ^a	−54.4874	−118.9355	58	80.99	6.0	6.0	0.13	3.5	201	25	45	58	63
141	Saint Exupery ^a	−62.2439	−155.4175	42	64.73	5.7	6.0	0.03	3.3	139	5	31	26	52
142	Tharp	−54.5941	−131.1230	462	78.82	6.6	6.7	0.09	9.9	4582	395	1026	234	298
143	Udintsev	−56.4114	−142.4340	325	74.49	6.4	6.6	0.11	8.6	2781	306	623	141	233
144	Vacquier ^a	−53.0360	−118.0905	52	82.29	5.8	6.0	0.13	3.3	170	21	38	34	57

SOUTHEAST INDIAN RIDGE

145	Amsterdam	−36.7018	78.6870	108	62.02	6.2	6.3	0.20	5.4	584	119	131	91	107
146	Balleny	−61.4293	154.8090	350	64.50	6.7	6.7	0.27	9.6	3340	916	748	269	255
147	Birubi ^a	−49.5044	127.2620	148	69.62	5.4	6.4	0.00	6.0	884	4	198	14	131
148	Boomerang ^a	−37.3610	78.2141	35	62.15	5.8	5.9	0.20	3.1	108	21	24	33	46
149	Euroka	−49.2295	126.0995	134	69.76	5.6	6.3	0.02	5.7	761	17	170	22	122
150	Geelvinck ^a	−41.9641	84.7104	303	65.60	5.5	6.6	0.01	8.8	2668	25	597	17	228
151	George V A	−51.3519	139.7170	235	67.49	6.5	6.5	0.26	7.6	1797	459	402	191	187
152	George V B	−53.2362	140.5525	179	67.30	5.8	6.4	0.04	6.7	1196	42	268	40	153
153	Heemskerck A ^a	−50.0051	115.5805	19	70.34	–	5.7	–	2.1	41	–	9	–	28
154	Heemskerck B ^a	−49.8762	115.9340	24	70.34	–	5.8	–	2.4	58	–	13	–	33
155	Heemskerck C ^a	−49.6495	116.1870	27	70.34	–	5.8	–	2.6	69	–	15	–	37
156	Heemskerck D ^a	−49.3967	116.4695	31	70.33	–	5.9	–	2.8	84	–	19	–	41
157	Hillegoms Hole ^a	−38.6621	78.3064	59	62.70	6.4	6.1	0.62	4.0	235	145	53	150	68
158	SEIR 100E	−47.6820	99.8058	129	69.46	6.5	6.3	0.30	5.6	721	218	161	189	118

Continued

TABLE 2 Predicted and Observed Seismicity on Mid-Ocean Ridge TransformFaults—Cont'd

Fault Segment #	Name	Latitude	Longitude	Length (km)	Slip Rate (mm/yr)	Max M_W	Max M_W exp.	χ	Width (km)	A_T (km ²)	A_E (km ²)	A_E pred. (km ²)	A_C (km ²)	A_C pred. (km ²)
159	SEIR 106E A ^a	−49.0854	106.2620	56	70.11	5.0	6.1	0.00	3.7	205	0	46	6	63
160	SEIR 106E B ^a	−48.6360	106.7910	59	70.12	5.5	6.1	0.03	3.8	222	7	50	16	66
161	SEIR 120 ^a	−49.4884	120.4165	154	70.19	5.3	6.4	0.00	6.1	935	1	209	11	135
162	SEIR 121 ^a	−49.3559	121.5315	80	70.13	5.3	6.2	0.02	4.4	350	5	78	11	83
163	SEIR 122 ^a	−49.7086	122.7255	50	70.04	5.3	6.0	0.01	3.5	173	1	39	12	58
164	SEIR 88E ^a	−41.9219	88.4153	65	66.47	5.8	6.1	0.12	4.0	264	32	59	39	72
165	SEIR 96E A	−45.6635	96.0315	89	68.69	6.4	6.2	0.36	4.7	416	148	93	157	90
166	SEIR 96E B ^a	−46.4296	96.1364	40	68.82	5.7	5.9	0.20	3.1	125	25	28	28	49
167	St Vincent ^a	−54.4960	144.1215	58	66.50	5.9	6.1	0.30	3.9	222	66	50	48	66
168	Tasman A	−55.2315	146.3335	90	66.05	6.9	6.2	0.66	4.8	431	283	96	401	92
169	Tasman B	−56.5921	147.2790	218	65.82	6.4	6.5	0.16	7.5	1626	263	364	152	178
170	Tasman C ^a	−57.7873	148.4671	62	65.51	6.5	6.1	0.68	4.0	247	167	55	196	69
171	Tasman D	−58.8662	149.2500	173	65.29	6.3	6.4	0.10	6.7	1154	118	258	118	150
172	Tasman E	−59.8753	150.5617	82	65.29	6.5	6.2	0.36	4.6	377	137	84	174	86
173	Ter Tholen ^a	−33.4444	77.7178	89	60.26	5.3	6.2	0.01	5.0	443	5	99	10	93
174	Vlamingh	−41.4712	80.3625	123	64.35	6.4	6.3	0.40	5.7	697	278	156	154	116
175	Warringa A ^a	−49.4070	123.3800	38	70.00	5.3	5.9	0.01	3.0	115	1	26	12	47
176	Warringa B ^a	−49.0728	123.8695	49	69.97	—	6.0	—	3.4	168	—	38	—	57
177	Zeehaen A ^a	−50.2303	114.0686	31	70.35	5.6	5.9	0.14	2.7	84	11	19	25	41
178	Zeehaen B ^a	−49.9722	114.2949	31	70.35	5.8	5.9	0.13	2.7	84	11	19	34	41
179	Zeewolf A ^a	−35.4438	78.4580	32	61.41	5.0	5.9	0.00	3.0	95	0	21	6	43
180	Zeewolf B ^a	−35.1800	78.6366	29	61.36	5.3	5.9	0.07	2.8	82	6	18	11	40

SOUTHWEST INDIAN RIDGE														
181	Andrew Bain A	−47.4907	32.2321	87	13.35	6.4	6.4	0.57	10.5	909	516	204	151	133
182	Andrew Bain B & C	−50.4204	29.6504	623	13.34	6.4	7.0	0.04	28.0	17,433	663	3903	130	582
183	Atlantis II	−32.7572	57.0414	201	12.02	5.8	6.7	0.02	16.8	3365	56	753	37	256
184	Bouvet	−54.2649	1.9220	201	12.72	6.6	6.7	0.29	16.3	3271	963	732	210	252
185	Discovery II A	−43.2960	41.6629	124	12.91	6.4	6.5	0.29	12.6	1573	450	352	139	175
186	Discovery II B	−41.8592	42.5948	216	12.89	6.7	6.7	0.25	16.7	3620	899	810	289	265
187	Du Toit	−53.0075	25.4810	130	13.29	6.2	6.5	0.13	12.8	1665	223	373	95	180
188	Eric Simpson	−43.7349	39.2474	89	13.03	6.7	6.4	0.62	10.7	952	594	213	270	136
189	Gallieni	−36.6370	52.3209	114	12.34	6.9	6.5	0.83	12.4	1418	1177	318	416	166
190	Gauss ^a	−34.9983	54.1242	59	12.23	6.2	6.3	0.43	9.0	530	231	119	84	102
191	Gazelle	−35.8023	53.4257	81	12.27	5.8	6.4	0.12	10.5	852	100	191	38	129
192	Indomed	−39.4741	46.1057	141	12.73	5.8	6.5	0.05	13.6	1921	105	430	38	193
193	Islas Orcadas	−54.1828	6.0992	100	12.85	6.1	6.4	0.22	11.5	1142	248	256	77	149
194	Marion	−46.4684	33.6623	109	13.22	6.2	6.4	0.20	11.8	1281	257	287	93	158
195	Melville	−29.8412	60.7767	92	11.74	6.9	6.4	1.39	11.5	1054	1468	236	465	143
196	Novara ^a	−31.4254	58.4107	45	11.93	–	6.2	–	7.9	357	–	80	–	83
197	Prince Edward	−45.4457	35.1282	146	13.19	6.4	6.5	0.31	13.6	1989	620	445	142	197
198	Shaka ^a	−53.5524	9.0237	199	12.92	6.8	6.6	0.40	16.1	3198	1284	716	376	249

^a Segment not included in scaling relation computation b/c it was too small or did not large enough earthquakes.

maximum earthquake size on RTFs. While insufficient resolution of the bathymetry data used to delineate fault structure may mean our updated RTF characterization is missing some step-overs $\geq \tilde{L}_S$ (where \tilde{L}_S is typically greater than ~ 5 km; [Wolfson-Schwehr et al., 2017](#)), observations from OBS data and tomographic studies on RTFs ([Van Avendonk et al., 2001](#); [Roland et al., 2012](#); [Froment et al., 2014](#)) indicate that the seismic deficit and small earthquake size are most likely related to significant along-strike variations in mechanical properties.

Structural features that suggest current or previous periods of transpression along an RTF segment are most likely to have an effect on the scaling relations; specifically, we expect compression to lead to higher seismic coupling (A_E/A_T) and maximum-sized earthquakes that rupture a greater portion of the fault (A_C/A_T) than the scaling relations would predict. The presence of median ridges, anomalously rotated abyssal hills, and transverse ridges are all indicators of current or past compression across the fault. On average, faults that have median ridges along the whole fault (8 segments) or have a combination of median ridge and median valley (8 segments) have 19% greater seismic coupling and largest earthquakes that rupture $\sim 22\%$ more total fault area than faults with only median valleys (78 segments). Where there was sufficient data resolution beyond the transform/ridge domain to note the presence or absence of associated structural features (126 faults), we found that faults with transverse ridges (52 segments) have the same average seismic coupling and largest earthquakes that rupture only 9% more fault compared to faults without transverse ridges (74 segments). Anomalously rotated abyssal hills were observed along three faults: Clipperton, Pitman, and Menard. Clipperton is the only one of these three faults that also has a median ridge and is the only one that has a significantly higher amount of seismic coupling and much larger maximum earthquakes than the scaling relations predict. Thus, anomalously rotated abyssal hills are not a strong indicator of the degree of the seismic coupling or the maximum earthquake size.

Structural features that indicate changes in plate motion, or evolution of the plate boundary, may also affect the seismic coupling and maximum earthquake sizes. We investigated the effect of the presence or lack of fracture zones on seismic coupling and the portion of the fault ruptured in the largest earthquake along the faults with sufficient data resolution outside the RTIs. The majority of RTF fault segments (168 segments) have discernable fracture zone traces and these faults have on average $\sim 17\%$ lower seismic coupling and largest earthquakes that ruptured $\sim 37\%$ less fault area, compared with the 15 RTF segments without fracture zones. One explanation for why faults without fracture zones would have higher seismic coupling and larger earthquakes than those with fracture zones may be that these faults are relatively young and still evolving, as in the case of the Discovery Transform Fault ([Pickle et al., 2009](#); [Wolfson-Schwehr et al., 2014](#)), or recent plate reorganization may have restructured the faults, as in the case of the Orozco Transform Fault ([Klitgord and Mammerickx, 1982](#)). In these cases, these faults might be more seismically active as they evolve and adjust to the surrounding stress regime and would therefore exert a stronger influence on the resulting scaling relations.

Some faults as shown in [Figs. 5 and 6](#) stand out as anomalous, either having significantly higher A_E or A_C than predicted, or both. We look more carefully at these RTFs to see if their anomalous seismic behavior can be related to the stress state inferred by the observed structural features. One example is the Clipperton Transform Fault (highlighted in [Fig. 6](#)) which hosts repeated M_W 6.6 earthquakes, vs the predicted M_W 6.1, and is characterized by 40% seismic coupling vs the predicted 22%. As previously noted, several lines of evidence suggest that

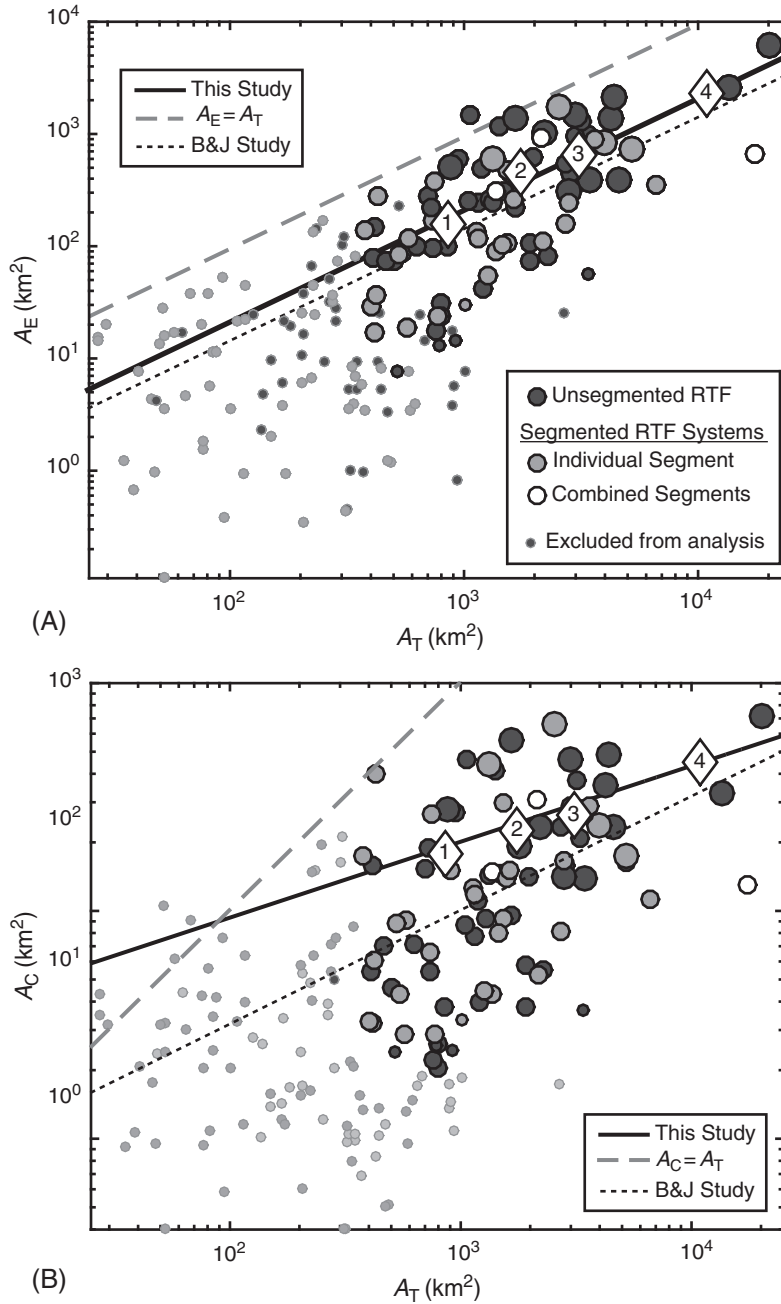


FIG. 5 (A) Effective seismogenic area, A_E , vs the seismogenic area, A_T , and (B) the area ruptured in the largest expected earthquake, A_C , vs A_T . The large, bold circles represent each RTF in our scaling relation analysis sized by the cumulative moment release. The small, light circles represent RTFs excluded from the analysis as described in the text. Colors denote segmentation: dark gray represents unsegmented RTFs, medium gray represents an individual fault segment that is part of a larger segmented RTF system, and white denotes a single through-going fault comprising two combined fault segments with an adjoining step-over length less than L_S . In both plots, the thick black line indicates the scaling relationship computed in this study. The dotted black line is the scaling relation of [Boettcher and Jordan \(2004\)](#). The dashed gray line shows the 1:1 scaling of $A_E: A_T$ and $A_C: A_T$, respectively.

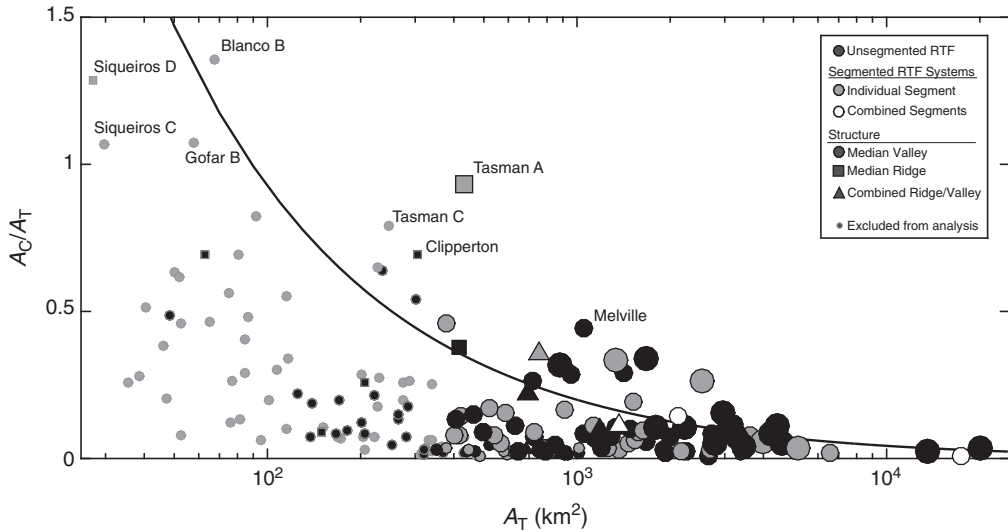


FIG. 6 Fraction of the fault ruptured in the largest earthquake, A_C/A_T , vs A_T . Black line represents the scaling relation for A_C computed for this study. Some of the anomalous fault segments have been labeled in this figure. Faults denoted by small lightly colored circles were not included in the analysis due to either being too small or not having large enough earthquakes. As in Fig. 5, colors denote segmentation: dark gray represents unsegmented RTFs, medium gray represents an individual fault segment that is part of a larger segmented RTF system, and white denotes a single through-going fault comprising two combined fault segments with an adjoining step-over length less than \tilde{L}_S . Shapes denote the structure of fault trace, whereas circles represent median valleys, squares denote median ridges, and triangles represent faults with a mixed ridge/valley.

the Clipperton Transform Fault has undergone repeated periods of transpression in the last few million years, which may still be affecting its seismicity and structure. Compression along Clipperton would increase normal stresses across the fault that may lead to larger stress drops, larger earthquakes, and higher seismic coupling (Boettcher and McGuire, 2009).

Tasman A and Tasman C, two segments of the Tasman Transform Fault system on the Southeast Indian Ridge (SEIR), are also anomalous relative to the scaling relations (Table 2, Fig. 6). The largest expected earthquake on Tasman A is an M_W 6.2. However, in 2007 an M_W 6.9 event occurred on the fault segment. The whole Tasman Transform Fault system is composed of five individual fault segments, with Tasman A being the only segment defined by a median ridge, suggesting compression. Tasman C also has a higher than the predicted maximum-sized earthquake (M_W 6.5 vs the predicted 6.0), yet this fault segment is defined by a median valley and appears to be under extension. Tasman C is a relatively short segment (61 km) compared to the lengths of Tasman B (218 km) and Tasman D (173 km). Consequently, the seismicity on Tasman C may be influenced by the proximity of the much larger adjacent segments. Although the step-overs separating Tasman C from Tasman B and D are greater than the critical step-over length, \tilde{L}_S , complete thermal decoupling between segments does not occur until $\sim 4\tilde{L}_S$ (Wolfson-Schwehr et al., 2017).

Therefore, Tasman C may have a larger A_T than predicted by the halfspace cooling model, in which case the value of A_C/A_T shown in Fig. 6 would be too high.

The Melville Transform Fault is a single segment fault composed of a mixed median valley/ridge on the SWIR that has higher than predicted maximum-sized earthquakes (M_W 6.9 vs M_W 6.4) and a significantly higher than predicted A_E . Fig. 5A suggests that seismic coupling on Melville is greater than 1.0. While it does not make sense to have a true seismic coupling greater than 1, this could occur in our calculation of seismic coupling if the seismic catalog (~ 41 years) captured incomplete seismic cycles, in which the number of the largest expected events captured is larger than the number of intervening quiet periods.

The segments Blanco B, Gofar B, Siqueiros C, and Siqueiros D are all small fault segments ($A_T < 100 \text{ km}^2$) that are part of much larger, seismically active, segmented fault systems that host $M_W \geq 6.0$ earthquakes (Fig. 6). As in the case of Tasman C, these small segments could have a larger A_T than predicted due to the proximity of the larger adjacent faults segments. It is also possible that the large events associated with these small fault segments are mislocated, and actually belong on one of the larger adjacent segments.

5 CONCLUSION

This study presents a global characterization of the physical structure and seismic behavior of oceanic transform faults. One of the primary goals of this study was to determine how prevalent physical segmentation of the fault trace is along the oceanic transform faults, and whether that segmentation significantly affects seismic behavior. The global characterization is based on the delineation of 204 individual fault segments, which are classified into 96 single-segment faults and 37 segmented fault systems. Segmentation was observed on transform faults offsetting ridges over the full range of spreading rates, with the highest prevalence of segmentation on the fast-slipping EPR. Plate-motion changes over the last couple of million years facilitated the segmentation of faults on the EPR via the formation of ITSCs.

This study also examined whether segmentation along ridge-bounded transform faults can explain the low seismic coupling and small maximum earthquake size that are a defining characteristic of RTF seismic behavior. Accounting for segmentation, by breaking up segmented RTF fault systems into their individual fault segments, only slightly increased both seismic coupling and the fraction of the fault ruptured by the largest earthquakes relative to previous analysis. Thus, while physical segmentation may contribute to the previously determined seismic deficit and small earthquakes observed on RTFs, along-strike changes in the material properties, frictional properties, and/or porosity most likely exert the strongest influence on RTF seismicity. These along-strike variations create fully coupled patches on RTFs, separated by partially coupled patches that host swarms of microseismicity and are barriers to large event rupture propagation. Improved resolution of seafloor bathymetry data, along with additional OBS studies, will allow us to further address questions related to seismic and tectonic processes on oceanic transform faults.

Acknowledgments

The authors acknowledge Jochen Braunmiller for providing critical feedback on this chapter, as well as João C. Duarte for compiling the book and providing additional comments. This material is based on work supported by NSF Grant OCE-1352565 (MSB) and NOAA Grant NA10NOS4000073 (MWS).

References

- Abercrombie, R.E., Ekström, G., 2001. Earthquake slip on oceanic transform faults. *Nature* 410 (6824), 74–77. <https://doi.org/10.1038/35065064>.
- Aderhold, K., Abercrombie, R.E., 2016. The 2015 Mw 7.1 earthquake on the Charlie-Gibbs transform fault: repeating earthquakes and multimodal slip on a slow oceanic transform. *Geophys. Res. Lett.* 43 (12), 6119–6128. <https://doi.org/10.1002/2016GL068802>.
- Becker, J.J., Sandwell, D.T., Smith, W.H.F., Braud, J., Binder, B., Depner, J., Fabre, D., Factor, J., Ingalls, S., Kim, S.-H., Ladner, R., Marks, K., Nelson, S., Pharaoh, A., Trimmer, R., Von Rosenberg, J., Wallace, G., Weatherall, P., 2009. Global bathymetry and elevation data at 30 arc seconds resolution SRTM30_PLUS. *Marine Geodesy* 32 (4), 355–371. <https://doi.org/10.1080/01490410903297766>.
- Bird, R.T., Naar, D.F., Larson, R.L., Searle, R.C., Scotese, C.R., 1998. Plate tectonic reconstructions of the Juan Fernandez microplate: transformation from internal shear to rigid rotation. *J. Geophys. Res.* 103 (B4), 7049–7067. <https://doi.org/10.1029/97JB02133>.
- Bird, P., Kagan, Y.Y., Jackson, D.D., 2002. Plate tectonics and earthquake potential of spreading ridges and oceanic transform faults. In: Stein, S., Freymueller, J.T. (Eds.), *Plate Boundary Zones*. American Geophysical Union, Washington, DC, pp. 203–218.
- Boettcher, M.S., Jordan, T.H., 2004. Earthquake scaling relations for mid-ocean ridge transform faults. *J. Geophys. Res.* 109 (B12), 74. <https://doi.org/10.1029/2004JB003110>.
- Boettcher, M.S., McGuire, J.J., 2009. Scaling relations for seismic cycles on mid-ocean ridge transform faults. *Geophys. Res. Lett.* 36 (21), 74. <https://doi.org/10.1029/2009GL040115>.
- Boettcher, M.S., Hirth, G., Evans, B., 2007. Olivine friction at the base of oceanic seismogenic zones. *J. Geophys. Res.* 112 (B1), 74. <https://doi.org/10.1029/2006JB004301>.
- Boettcher, M.S., McGarr, A., Johnston, M., 2009. Extension of Gutenberg-Richter distribution to MW-1.3, no lower limit in sight. *Geophys. Res. Lett.* 36(L10307). <https://doi.org/10.1029/2009GL038080>.
- Braunmiller, J., Nábělek, J., 2008. Segmentation of the Blanco Transform Fault Zone from earthquake analysis: complex tectonics of an oceanic transform fault. *J. Geophys. Res.* 113 (B7), 74. <https://doi.org/10.1029/2007JB005213>.
- Brune, J.N., 1968. Seismic moment, seismicity, and rate of slip along major fault zones. *J. Geophys. Res.* 73 (2), 777–784. <https://doi.org/10.1029/jb073i002p00777>.
- Carbotte, S.M., Macdonald, K., 1994. Comparison of seafloor tectonic fabric at intermediate, fast, and super fast spreading ridges: influence of spreading rate, plate motions, and ridge segmentation on fault patterns. *J. Geophys. Res.* 99(B7). <https://doi.org/10.1029/93JB02971>.
- Coffin, M.F., Gahagan, L.M., Lawver, L.A., 1998. Present-day plate boundary digital data compilation: University of Texas Institute for Geophysics Technical Report. No. 174.
- Cowan, D.S., Botros, M., Johnson, H.P., 1986. Bookshelf tectonics: rotated crustal blocks within the Sovanco Fracture Zone. *Geophys. Res. Lett.* 13 (10), 995–998. <https://doi.org/10.1029/GL013i010p00995>.
- Croon, M.B., Cande, S.C., Stock, J.M., 2010. Abyssal hill deflections at Pacific-Antarctic ridge-transform intersections. *Geochem. Geophys. Geosyst.* 11Q11004. <https://doi.org/10.1029/2010gc003236>.
- Dick, H.J.B., Lin, J., Schouten, H., 2003. An ultraslow-spreading class of ocean ridge. *Nature* 426 (6965), 405–412. <https://doi.org/10.1038/nature02128>.
- Dietz, R.S., Menard, H.W., and Hamilton, E.L., 1954. Echograms of the Mid-Pacific expedition: Deep Sea Res. (1953), v. 1, no. 4, p. 258IN3267–266IN4272, [https://doi.org/10.1016/0146-6313\(54\)90008-8](https://doi.org/10.1016/0146-6313(54)90008-8).
- Dziak, R.P., Fox, C.G., Embley, R.W., Nabelek, J.L., Braunmiller, J., Koski, R.A., 2000. Recent tectonics of the Blanco Ridge, eastern Blanco Transform Fault Zone. *Marine Geophys. Res.* 21 (5), 423–450. <https://doi.org/10.1023/A:1026545910893>.
- Dziewonski, A.M., Anderson, D.L., 1981. Preliminary reference Earth model. *Phys. Earth Planet. Inter.* 25 (4), 297–356. [https://doi.org/10.1016/0031-9201\(81\)90046-7](https://doi.org/10.1016/0031-9201(81)90046-7).

- Ekström, G., Nettles, M., Dziewoński, A.M., 2012. The global CMT project 2004–2010: centroid-moment tensors for 13,017 earthquakes. *Phys. Earth Planet. Inter.* 200, 1–9. <https://doi.org/10.1016/j.pepi.2012.04.002>.
- Embley, R.W., Wilson, D.S., 1992. Morphology of the Blanco Transform Fault Zone-NE Pacific: Implications for its tectonic evolution. *Mar. Geophys. Res.* 14 (1), 25–45. <https://doi.org/10.1007/BF01674064>.
- Fornari, D.J., Gallo, D.G., Edwards, M.H., Madsen, J.A., Perfit, M.R., Shor, A.N., 1989. Structure and topography of the Siqueiros transform fault system: Evidence for the development of intra-transform spreading centers. *Mar. Geophys. Res.* 11 (4), 263–299. <https://doi.org/10.1007/BF00282579>.
- Forsyth, D.W., Kerber, L., and Pickle, R., 2007. Co-existing overlapping-spreading-center and ridge-transform Geometry: Eos Trans. AGU, 88(52), Fall Meet. Suppl., Abstract T32B–05.
- Fox, P.J., Gallo, D.G., 1984. A tectonic model for ridge-transform-ridge plate boundaries: implications for the structure of oceanic lithosphere. *Tectonophysics* 104 (3–4), 205–242. [https://doi.org/10.1016/0040-1951\(84\)90124-0](https://doi.org/10.1016/0040-1951(84)90124-0).
- Fox, P.J., Gallo, D.G., 1989. Transforms of the Eastern Pacific. In: Winterer, E.L., Hussong, D.M., Decker, R.W. (Eds.), *The Eastern Pacific Ocean and Hawaii*. Geological Society of America, Boulder, CO, pp. 111–124.
- Frolich, C., Wetzel, L.R., 2007. Comparison of seismic moment release rates along different types of plate boundaries. *Geophys. J. Int.* 171 (2), 909–920. <https://doi.org/10.1111/j.1365-246X.2007.03550.x>.
- Froment, B., McGuire, J.J., Hilst, R.D., Gouédard, P., Roland, E.C., Zhang, H., Collins, J.A., 2014. Imaging along-strike variations in mechanical properties of the Gofar transform fault, East Pacific Rise. *J. Geophys. Res. Solid Earth* 119 (9), 7175–7194. <https://doi.org/10.1002/2014JB011270>.
- Gallo, D.G., Fox, P.J., Macdonald, K.C., 2012. A Sea Beam investigation of the Clipperton Transform Fault: the morphotectonic expression of a fast slipping transform boundary. *J. Geophys. Res.* 91 (B3), 3455–3467. <https://doi.org/10.1029/JB091iB03p03455>.
- Goff, J.A., Fornari, D.J., Cochran, J.R., Keeley, C., Malinverno, A., 1993. Wilkes transform system and “nannoplate” *Geology* 21 (7), 623–626. [https://doi.org/10.1130/0091-7613\(1993\)021<0623:WTSAN>2.3.CO;2](https://doi.org/10.1130/0091-7613(1993)021<0623:WTSAN>2.3.CO;2).
- Gregg, P.M., Lin, J., Smith, D.K., 2006. Segmentation of transform systems on the East Pacific Rise: implications for earthquake processes at fast-slipping oceanic transform faults. *Geology* 34 (4), 289. <https://doi.org/10.1130/g22212.1>.
- Gregg, P.M., Behn, M.D., Lin, J., Grove, T.L., 2009. Melt generation, crystallization, and extraction beneath segmented oceanic transform faults. *J. Geophys. Res.* 114 (B11), 115. <https://doi.org/10.1029/2008JB006100>.
- Hey, R., 1977. A new class of “pseudofaults” and their bearing on plate tectonics: a propagating rift model. *Earth Planet. Sci. Lett.* 37 (2), 321–325. [https://doi.org/10.1016/0012-821X\(77\)90177-7](https://doi.org/10.1016/0012-821X(77)90177-7).
- Kagan, Y.Y., Jackson, D.D., 2000. Probabilistic forecasting of earthquakes. *Geophys. J. Int.* 143 (2), 438–453. <https://doi.org/10.1046/j.1365-246X.2000.01267.x>.
- Kastens, K.A., Macdonald, K.C., Becker, K., Crane, K., 1979. The Tamayo transform fault in the mouth of the Gulf of California. *Mar. Geophys. Res.* 4 (2), 129–151. <https://doi.org/10.1007/BF00286401>.
- King, D., Marone, C., 2012. Frictional properties of olivine at high temperature with applications to the strength and dynamics of the oceanic lithosphere. *J. Geophys. Res.* 117 (B12203). <https://doi.org/10.1029/2012JB009511>.
- Klitgord, K.D., Mammerickx, J., 1982. Northern East Pacific Rise: magnetic anomaly and bathymetric framework. *J. Geophys. Res.* 87 (B8), 6725–6750. <https://doi.org/10.1029/JB087iB08p06725>.
- Kreemer, C., Haines, J., Holt, W.E., Blewitt, G., Lavalée, D., 2000. On the determination of a global strain rate model. *Earth Planets Space* 52, 765–770. <https://doi.org/10.1186/BF03352279>.
- Kuna, V., Nábelek, J., Braunmiller, J., 2017. Mode of seismic slip at an Ocean Transform Fault: Results from the Blanco Transform Fault OBS Experiment. Abstract T51G-0562 presented at the 2017 Fall Meeting, AGU, New Orleans, LA, 11–15 Dec.
- Liu, Y., McGuire, J.J., Behn, M.D., 2012. Frictional behavior of oceanic transform faults and its influence on earthquake characteristics. *J. Geophys. Res.* 117 (B04315), B04315. <https://doi.org/10.1029/2011JB009025>.
- Lonsdale, P., 1978. Near-bottom reconnaissance of a fast-slipping transform fault zone at the Pacific-Nazca plate boundary. *J. Geol.* 86 (4), 451–472. <https://doi.org/10.1086/649712>.
- Lonsdale, P., 1994. Structural geomorphology of the eltanin fault system and adjacent transform faults of the Pacific-Antarctic plate boundary. *Mar. Geophys. Res.* 16 (2), 105–143. <https://doi.org/10.1007/BF01224756>.
- Macdonald, K.C., Kastens, K.A., Spiess, F.N., Miller, S.P., 1979. Deep tow studies of the Tamayo transform fault. *Mar. Geophys. Res.* 4 (1), 37–70. <https://doi.org/10.1007/BF00286145>.
- Macdonald, K., Sempéré, J.C., Fox, P.J., 1984. East Pacific Rise from Siqueiros to Orozco fracture zones: along-strike continuity of axial neovolcanic zone and structure and evolution of overlapping spreading centers. *J. Geophys. Res.* 89 (B7), 6049–6069. <https://doi.org/10.1029/JB089iB07p06049>.

- Macdonald, K.C., Fox, P.J., Miller, S., Carbotte, S.M., Edwards, M.H., Eisen, M.F., Fornari, D.J., Perram, L., Pockalny, R.A., Scheirer, D.S., Tighe, S., Weiland, C., Wilson, D., 1992. The East Pacific Rise and its flanks 8–18° N: history of segmentation, propagation and spreading direction based on SeaMARC II and Sea Beam Studies. *Mar. Geophys. Res.* 14 (4), 299–344. <https://doi.org/10.1007/BF01203621>.
- Madsen, J.A., Fox, P.J., Macdonald, K.C., 1986. Morphotectonic fabric of the Orozco Transform Fault: results from a Sea Beam investigation. *J. Geophys. Res. Solid Earth* (1978–2012) 91 (B3), 3439–3454. <https://doi.org/10.1029/JB091iB03p03439>.
- McGuire, J.J., 2008. Seismic cycles and earthquake predictability on East Pacific Rise transform faults. *Bull. Seismol. Soc. America* 98 (3), 1067–1084. <https://doi.org/10.1785/0120070154>.
- McGuire, J.J., Collins, J.A., Gouédard, P., Roland, E.C., Lizarralde, D., Boettcher, M.S., Behn, M.D., van der Hilst, R.D., 2012. Variations in earthquake rupture properties along the Gofar transform fault East Pacific Rise. *Nat. Geosci.* 5 (5), 336–341. <https://doi.org/10.1038/ngeo1454>.
- Menard, H.W., Atwater, T., 1968. Changes in direction of sea floor spreading. *Nature* 219 (5153), 463–467. <https://doi.org/10.1038/219463a0>.
- Moyer, P.A., Boettcher, M.S., McGuire, J.J., 2017. Spatial and temporal variations in earthquake stress drop on Gofar Transform Fault, East Pacific Rise. Implications for fault strength, Abstract S31C-0826 presented at the 2017 Fall Meeting, AGU, New Orleans, LA, 11–15 Dec.
- Murton, B.J., 1986. Anomalous oceanic lithosphere formed in a leaky transform fault: evidence from the Western Limassol Forest complex Cyprus. *J. Geol. Soc.* 143 (5), 845–854. <https://doi.org/10.1144/gsjgs.143.5.0845>.
- Parson, L.M., Searle, R.C., 1986. Strike-slip fault styles in slow-slipping oceanic transform faults—evidence from GLORIA surveys of Atlantis and Romanche Fracture Zones. *J. Geol. Soc.* 143 (5), 757–761. <https://doi.org/10.1144/gsjgs.143.5.0757>.
- Pickle, R.C., Forsyth, D.W., Harmon, N., Nagle, A.N., Saal, A., 2009. Thermo-mechanical control of axial topography of intra-transform spreading centers. *Earth Planet. Sci. Lett.* 284 (3–4), 343–351. <https://doi.org/10.1016/j.epsl.2009.05.004>.
- Pockalny, R.A., 1997. Evidence of transpression along the clipperton transform: implications for processes of plate boundary reorganization. *Earth Planet. Sci. Lett.* 146 (3–4), 449–464. [https://doi.org/10.1016/S0012-821X\(96\)00253-1](https://doi.org/10.1016/S0012-821X(96)00253-1).
- Pockalny, R.A., Gente, P., Buck, W.R., 1996. Oceanic transverse ridges: a flexural response to fracture-zone-normal extension. *Geology* 24 (1), 71–74. [https://doi.org/10.1130/0091-7613\(1996\)024<0071:OTRAFR>2.3.CO;2](https://doi.org/10.1130/0091-7613(1996)024<0071:OTRAFR>2.3.CO;2).
- Pockalny, R.A., Fox, P.J., Fornari, D.J., Macdonald, K.C., Perfit, M.R., 1997. Tectonic reconstruction of the clipperton and Siqueiros Fracture Zones: evidence and consequences of plate motion change for the last 3 Myr. *J. Geophys. Res.* 102 (B2), 3167–3181. <https://doi.org/10.1029/96JB03391>.
- Roland, E.C., McGuire, J.J., 2009. Earthquake swarms on transform faults. *Geophys. J. Int.* 178 (3), 1677–1690. <https://doi.org/10.1111/j.1365-246X.2009.04214.x>.
- Roland, E.C., Behn, M.D., Hirth, G., 2010. Thermal-mechanical behavior of oceanic transform faults: implications for the spatial distribution of seismicity. *Geochem. Geophys. Geosyst.* 11(7). <https://doi.org/10.1029/2010GC003034>.
- Roland, E.C., Lizarralde, D., McGuire, J.J., Collins, J.A., 2012. Seismic velocity constraints on the material properties that control earthquake behavior at the Quebrada-Discovery-Gofar transform faults, East Pacific Rise. *J. Geophys. Res.* 117 (B11102), B11102. <https://doi.org/10.1029/2012JB009422>.
- Ryan, W.B.F., Carbotte, S.M., Coplan, J.O., O'Hara, S., Melkonian, A., Arko, R., Weissel, R.A., Ferrini, V., Goodwillie, A., Nitsche, F., Bonczkowski, J., Zemsky, R., 2009. Global multi-resolution topography synthesis: geochemistry. *Geophys. Geosyst.* 10Q03014 <https://doi.org/10.1029/2008GC002332>.
- Sandwell, D.T., 1986. Thermal stress and the spacings of transform faults. *J. Geophys. Res.* 91 (B6), 6405–6418. <https://doi.org/10.1029/JB091iB06p06405>.
- Sandwell, D.T., Müller, R.D., Smith, W.H.F., Garcia, E., Francis, R., 2014. Marine geophysics new global marine gravity model from CryoSat-2 and Jason-1 reveals buried tectonic structure. *Science* 346 (6205), 65–67. <https://doi.org/10.1126/science.1258213>.
- Searle, R., 1984. Gloria survey of the east pacific rise near 3.5°S tectonic and volcanic characteristics of a fast spreading mid-ocean rise. *Tectonophysics* 101 (3–4), 319–344. [https://doi.org/10.1016/0040-1951\(84\)90119-7](https://doi.org/10.1016/0040-1951(84)90119-7).
- Searle, R.C., 1986. GLORIA investigations of oceanic fracture zones: comparative study of the transform fault zone. *J. Geol. Soc.* 143 (5), 743–756. <https://doi.org/10.1144/gsjgs.143.5.0743>.

- Smith, W.H.F., Sandwell, D.T., 1997. Global sea floor topography from satellite altimetry and ship depth soundings. *Science* 277 (5334), 1956–1962. <https://doi.org/10.1126/science.277.5334.1956>.
- Sonder, L.J., Pockalny, R.A., 1999. Anomalous rotated abyssal hills along active transforms: distributed deformation of oceanic lithosphere. *Geology* 27 (11), 1003–1006. [https://doi.org/10.1130/0091-7613\(1999\)027<1003:ARAHAA>2.3.CO;2](https://doi.org/10.1130/0091-7613(1999)027<1003:ARAHAA>2.3.CO;2).
- Sykes, L.R., Ekström, G., 2012. Earthquakes along Eltanin transform system SE Pacific Ocean: fault segments characterized by strong and poor seismic coupling and implications for long-term earthquake prediction. *Geophys. J. Int.* 188 (2), 421–434. <https://doi.org/10.1111/j.1365-246X.2011.05284.x>.
- Taylor, B., Crook, K., Sinton, J., 1994. Extensional transform zones and oblique spreading centers. *J. Geophys. Res.* 99 (B10), 19707–19718. <https://doi.org/10.1029/94JB01662>.
- Van Avendonk, H.J.A., Harding, A.J., Orcutt, J.A., McClain, J.S., 2001. Contrast in crustal structure across the Clipperton transform fault from travel time tomography. *J. Geophys. Res. Solid Earth* (1978–2012) 106 (B6), 10961–10981. <https://doi.org/10.1029/2000JB900459>.
- Willoughby, E.C., Hyndman, R.D., 2005. Earthquake rate, slip rate, and the effective seismic thickness for oceanic transform faults of the Juan de Fuca plate system. *Geophys. J. Int.* 160 (3), 855–868. <https://doi.org/10.1111/j.1365-246X.2005.02523.x>.
- Wilson, J.T., 1965a. A new class of faults and their bearing on continental drift. *Nature* 207 (4995), 343–347. <https://doi.org/10.1038/207343a0>.
- Wilson, J.T., 1965b. Transform faults, oceanic ridges, and magnetic anomalies southwest of Vancouver Island. *Science* 150 (3695), 482–485. <https://doi.org/10.1126/science.150.3695.482>.
- Wolfson-Schwehr, M., Boettcher, M.S., McGuire, J.J., Collins, J.A., 2014. The relationship between seismicity and fault structure on the Discovery transform fault, East Pacific Rise. *Geochem. Geophys. Geosyst.* 15 (9), 3698–3712. <https://doi.org/10.1002/2014GC005445>.
- Wolfson-Schwehr, M., Boettcher, M.S., Behn, M.D., 2017. Thermal segmentation of mid-ocean ridge-transform faults. *Geochem. Geophys. Geosyst.* 410 (6824), 74. <https://doi.org/10.1002/2017GC006967>.

Further Reading

- Behn, M.D., Boettcher, M.S., Hirth, G., 2007. Thermal structure of oceanic transform faults. *Geology* 35 (4), 307–310. <https://doi.org/10.1130/G23112A.1>.
- Moyer, P., Boettcher, M.S., McGuire, J.J., Collins, J.A., 2015. Constraining Earthquake Source Parameters in Rupture Patches and Rupture Barriers on Gofar Transform Fault, East Pacific Rise From Ocean Bottom Seismic Data. Abstract S51A-2635 presented at the 2015 Fall Meeting, AGU, San Francisco, CA, 14–18 Dec.
- Smith, W.H.F., 1998. Seafloor tectonic fabric from satellite altimetry. *Annu. Rev. Earth Planet. Sci.* 26 (1), 697–747. <https://doi.org/10.1029/91EO10017>.